THE ASTROPHYSICAL JOURNAL, 648:435–451, 2006 September 1

DUST DESTRUCTION IN THE HIGH-VELOCITY SHOCKS DRIVEN BY SUPERNOVAE IN THE EARLY UNIVERSE

TAKAYA NOZAWA[1] AND TAKASHI KOZASA[1]
Division of Earth and Planetary Sciences, Graduate School of Science, Hokkaido University, Sapporo 060-0810, Japan;
nozawa@ep.sci.hokudai.ac.jp, kozasa@ep.sci.hokudai.ac.jp

AND

ASAO HABE[1]
Division of Physics, Graduate School of Science, Hokkaido University, Sapporo 060-0810, Japan; habe@astro1.sci.hokudai.ac.jp
Received 2006 March 11; accepted 2006 May 5

ABSTRACT

We investigate the destruction of dust grains by sputtering in the high-velocity interstellar shocks driven by supernovae (SNe) in the early universe to reveal the dependence of the timescale of dust destruction on the gas density $n_{\rm H,0}$ in the interstellar medium (ISM), as well as on the progenitor mass $M_{\rm pr}$ and explosion energy E_{51} of SNe. The sputtering yields for the combinations of dust and ion species of interest to us are evaluated by applying the so-called universal relation with a slight modification. The dynamics of dust grains and their destruction by sputtering in shocks are calculated by taking into account the size distribution of each dust species, together with the time evolution of the temperature and density of the gas in spherically symmetric shocks. The results of the calculations show that the efficiency of dust destruction depends not only on the sputtering yield but also on the initial size distribution of each grain species. The efficiency of dust destruction increases with increasing E_{51} and/or increasing $n_{\rm H,0}$ but is almost independent of $M_{\rm pr}$ as long as E_{51} is the same. The mass of gas swept up by a shock is an increasing function of E_{51} and a decreasing function of $n_{\rm H,0}$. Combining these results, we present the approximation formula for the timescale of destruction for each grain species in the early universe as a function of E_{51} and $n_{\rm H,0}$. This formula is applicable for investigating the evolution of dust grains at the early epoch of the universe with the metallicity of $Z \lesssim 10^{-3}\,Z_\odot$. The effects of the cooling processes of gas on the destruction of dust are briefly discussed.

Subject headings: dust, extinction — early universe — shock waves — supernova remnants — supernovae: general

Online material: color figures

1. INTRODUCTION

Population III stars formed from metal-free gas clouds where the H_2 molecule is the main coolant of gas are considered to be more massive than $10^2\,M_\odot$ (Bromm & Larson 2004 and references therein), although there are still numerous uncertainties regarding the mass range of the first stars due to a poor understanding of the relevant radiative feedback in the late accretion phase (see, e.g., Tan & McKee 2004). Once the primordial gas is enriched by dust grains, dust has a great influence on the subsequent formation and evolution history of stars and galaxies; the star formation rate (SFR) in the metal-poor star-forming clouds is enhanced via the formation of H_2 molecules on the surface of dust grains (Hirashita & Ferrara 2002; Cazaux & Spaans 2004). In addition, the cooling of gas by thermal radiation from dust itself makes even the gas clouds with metallicity as low as $10^{-5}\,Z_\odot$ fragment into low-mass gas clumps (Schneider et al. 2002, 2003; Omukai et al. 2005). Thus, dust grains in the early universe may cause the characteristic mass scale of stars to shift from very high mass to the low mass of $\sim 1\,M_\odot$ observed at the present time and strongly affect the evolution of the initial mass function (IMF) at the early epoch of the universe.

In addition, dust grains in the early universe play crucial roles in revealing the structure and evolution of the universe from the relevant observations because they absorb stellar light and re-emit it at infrared (IR) and submillimeter wavelengths. The thermal emission from dust at high redshifts can distort the cosmic microwave background (CMB) radiation (Loeb & Haiman 1997), and the obscuration and reddening of starlight by dust residing in the early interstellar and/or intergalactic space lead to a serious underestimate in evaluating the cosmic SFR from the observations directed toward higher redshifts (e.g., Hauser & Dwek 2001).

In fact, recent observations have confirmed the presence of large amounts of dust grains at high redshifts of $z \gtrsim 5$. The submillimeter (Priddey et al. 2003; Robson et al. 2004) and millimeter (Bertoldi et al. 2003) observations have reported continuum thermal emission of dust grains from some quasars at $z > 5$ and have suggested a large amount of cold dust reaching up to 10^8–$10^9\,M_\odot$ in the host galaxies of quasars. Maiolino et al. (2004a) discovered the substantial extinction of stellar light by dust in broad absorption line (BAL) quasars at $z > 4.9$. They have shown that their extinction curves could be different from those of low-redshift quasars at $z < 4$ and have suggested that the difference may reflect different formation and evolution mechanisms of dust grains at $z \gtrsim 5$.

The main sources of dust grains in the early universe at $z > 5$ are believed to be supernovae (SNe) evolving from the massive stars because of their short lifetime. Dust grains formed in the ejecta of SNe are injected into the interstellar medium (ISM) and are subjected to destructive processes in the interstellar shocks induced by the ambient SNe (e.g., Jones et al. 1994; Dwek et al. 1996). Thus, the size distribution and amount of dust in early interstellar space are determined by the balance between their

[1] Current address: Department of Cosmosciences, Graduate School of Science, Hokkaido University, Sapporo 060-0810, Japan.

production in SNe and their destruction in shocks, and they change with time according to the star formation activity (e.g., Dwek 1998).

The amount of dust that is destroyed in shocks, as well as how much of stellar light is absorbed and reemitted through thermal emission by dust grains, heavily depends on their chemical composition, size, and amount. Thus, it is essential to clarify the evolution of dust in the early universe by treating the formation and destruction processes of dust grains in a consistent manner, in order to elucidate the SFR and the IMF during the early evolution of the universe from future observations. Nozawa et al. (2003) investigated the chemical composition, size distribution, and amount of dust grains formed in the ejecta of Population III SNe. In this paper, as the second step to revealing the evolution of dust grains in the early universe, we explore dust destruction in the high-velocity interstellar shock driven by the SN explosion, adopting the dust model by Nozawa et al. (2003) for the initial dust residing in the early ISM.

We focus on dust destruction in a nonradiative shock where dust grains are considered to be efficiently destroyed by nonthermal and thermal sputtering (e.g., McKee 1989) because the nonradiative shock has a high shock velocity (>100 km s^{-1}) and a high gas temperature (>10^6 K). However, only a few sets of experimental data on sputtering yield are available for the projectile-target combinations of astrophysical interest. Hence, we first evaluate the sputtering yields for the combinations of dust species produced in Population III SNe and ion species of interest to us, collecting a large amount of sputtering data and applying the universal relation for sputtering yield proposed by Bohdansky (1984) with a slight modification so as to reproduce the experimental data well. Then we investigate the dependence of the efficiency of dust destruction for each grain species not only on the gas density $n_{\rm H,0}$ in the ISM but also on the explosion energy E_{51} and progenitor mass $M_{\rm pr}$ of the SN driving the interstellar shocks by applying the hydrodynamic models of Population III SNe by Umeda & Nomoto (2002). Finally, we evaluate the timescale of destruction for each grain species.

The efficiency of dust destruction by sputtering depends on the temperature and density of the gas and the velocity of dust relative to gas in the shock, as well as the sputtering yield and the dust size. Thus, in the calculation, we solve the time evolution of the temperature and density of gas in spherically symmetric shocks, including the cooling of gas by the atomic process, inverse Compton scattering, and the thermal emission of dust. Together with the hydrodynamic calculations for gas, we carefully treat the erosion of dust by thermal and nonthermal sputtering caused by the motion of dust relative to gas, taking into account the size distribution of each dust species.

This paper is organized as follows: We first define the efficiency of dust destruction in § 2. In § 3, we describe the properties of the ISM in the early universe, together with the dust model adopted in the calculations, and in § 4, we present the basic equations of the hydrodynamic calculations for gas and the method of the simulation for dust destruction in the shock. The sputtering yield of each grain species necessary for the calculations of dust destruction is evaluated in § 5, and the grain physics in the shock is described in § 6. The results of calculations of dust destruction are given in detail for the model of interstellar shock that is driven by a SN with $E_{51} = 1$ and $M_{\rm pr} = 20\ M_\odot$ and is propagating into the ISM with $n_{\rm H,0} = 1$ $\rm cm^{-3}$, and the approximation formula for the timescale of dust destruction as a function of E_{51} and $n_{\rm H,0}$ is derived in § 7, where the effects of the cooling of gas on the evolution of nonradiative shock and the destruction of dust are briefly discussed. The summary is presented in § 8.

2. THE DEFINITION OF THE EFFICIENCY OF DUST DESTRUCTION

Our main goal is to reveal the timescale of dust destruction by interstellar shocks in the early universe. In general, the timescale of destruction $\tau_{{\rm SN},j}$ for grain species j is defined as (e.g., McKee 1989)

$$\tau_{{\rm SN},j}^{-1} = \epsilon_j \frac{M_{\rm swept}}{M_{\rm ISM}} \gamma_{\rm SN}, \tag{1}$$

where ϵ_j is the efficiency of destruction of grain species j, $M_{\rm swept}$ is the mass of gas swept up by a shock until the shock velocity $V_{\rm shock}$ decelerates below 100 km s^{-1}, $M_{\rm ISM}$ is the mass of gas and dust in the ISM, and $\gamma_{\rm SN}$ is the effective SN rate. McKee (1989) has estimated ϵ_j to be nearly constant and found that $M_{\rm swept}$ is proportional to the SN explosion energy E_{51} in units of 10^{51} ergs. However, it is expected that both ϵ_j and $M_{\rm swept}$ depend on not only E_{51} but also the progenitor mass $M_{\rm pr}$ of the SN and the number density of gas $n_{\rm H,0}$ in the ISM. Hence, we aim at deriving the dependences of ϵ_j and $M_{\rm swept}$ on E_{51}, $M_{\rm pr}$, and $n_{\rm H,0}$. The truncation time $t_{\rm tr}$ being defined as the time at which $V_{\rm shock}$ drops down to 100 km s^{-1}, the efficiency of destruction ϵ_j for each dust species is calculated by

$$\epsilon_j = \frac{M_{d,j}^{\rm dest}(t = t_{\rm tr})}{M_{d,j}^{\rm swept}(t = t_{\rm tr})}, \tag{2}$$

where $M_{d,j}^{\rm dest}(t)$ and $M_{d,j}^{\rm swept}(t)$ are, respectively, the mass of dust destroyed and the mass of dust swept up by the shock, and the mass of gas $M_{\rm swept}$ swept up by a spherically symmetric shock is given by

$$M_{\rm swept} \simeq \frac{4\pi}{3} \rho_0 R_{\rm shock}^3(t = t_{\rm tr}), \tag{3}$$

with ρ_0 being the gas density in the ISM and $R_{\rm shock}(t)$ the travel distance of the shock front.

3. PROPERTIES OF THE ISM IN THE EARLY UNIVERSE

3.1. *Density, Temperature, and Metallicity of the ISM*

We assume that the ISM in the early universe is homogeneous and stationary ($v = 0$), referring to the results of the simulations on the formation of the early H II regions by the first stars (Kitayama et al. 2004), which have shown that the radiative feedback from the massive stars causes the ambient ISM to be homogenized with a mean gas density of $\lesssim 1$ $\rm cm^{-3}$. In the calculations, we consider the range of hydrogen number density in the ISM to be 0.03 $\rm cm^{-3} \leq n_{\rm H,0} \leq 10$ $\rm cm^{-3}$, in order to reveal the dependence of the efficiency of dust destruction on the gas density in the ISM. The ISM surrounding the SN explosion is considered to be ionized by the radiation of the massive progenitor stars and heated to $T_0 \sim 10^4$ K (Kitayama et al. 2004; Machida et al. 2005), and then T_0 is expected to decrease below 10^4 K, where the recombination rate can be high even for a metallicity as low as $Z = 10^{-4}\ Z_\odot$ (Wolfire et al. 1995). However, the evolution of the gas temperature in the postshock flow is almost independent of T_0 until the end of the Sedov-Taylor phase of the high-velocity shock considered in this paper, and the temperature of gas $T_{\rm shock}$ at the shock front does not decrease below several times 10^4 K at the truncation time, as is shown in the result of the calculations (see § 7.1). Thus, we take $T_0 = 10^4$ K as the representative gas temperature in the ISM, independently of the density of the gas.

The truncation time, as well as the time evolution of gas temperature and density structures in the postshock flow, is considered to be affected by the cooling of gas depending on the metallicity of the ISM. In particular, when $T_{\rm shock} \lesssim 10^5$ K, the efficient line coolings of H and He ions cause the shock velocity to decelerate rapidly and as a result regulate the truncation time. However, the gas cooling function is almost independent of the metallicity for $Z \lesssim 10^{-3}\ Z_\odot$ corresponding to [Fe/H] ≤ -3, since the metal lines do not contribute to the cooling of gas at $T \geq 10^4$ K (Sutherland & Dopita 1993), and we adopt the gas cooling function for the zero metal case given in Sutherland & Dopita (1993) (see § 4.1). Note that the efficiency of dust destruction, which is defined by the mass ratio of dust destroyed to dust swept up by the shock, does not depend on the metallicity as long as $Z \lesssim 10^{-3}\ Z_\odot$, despite the fact that the amount of dust in the ISM is proportional to the metallicity, and in the calculations we assume that the metallicity of the ISM in the early universe is $Z = 10^{-4}\ Z_\odot$ to investigate the destruction of dust in the ISM. The elemental composition of gas in the ISM is given in Table 1, where the C, N, and O metals are included so as to adjust the metallicity to $Z = 10^{-4}\ Z_\odot$ and their abundances are simply evaluated by multiplying the metallicity by the primordial ratios tabulated in Sutherland & Dopita (1993); note that these metals play no role in the physical processes relevant to dust destruction because of the much lower abundances than those of H and He. The electron number density n_e is fixed to $1.128 n_{\rm H}$ given by Sutherland & Dopita (1993).

TABLE 1
ELEMENTAL ABUNDANCES OF GAS IN THE ISM

$Z/Z_\odot$	$A_{\rm He}$	$A_{\rm C}$	$A_{\rm N}$	$A_{\rm O}$	A_e
10^{-4}.........	8.04×10^{-2}	3.62×10^{-8}	1.12×10^{-8}	2.70×10^{-7}	1.128

NOTES.—The number abundance A_i relative to that of the hydrogen atom in the ISM. Note that the abundances of C, N, and O are calculated by multiplying the metallicity of $Z = 10^{-4}\ Z_\odot$ by the primordial ratios in Table 4 of Sutherland & Dopita (1993).

3.2. *Model of Dust in the Early Universe*

Dust grains in the ISM at the early epoch of the universe considered in this paper are expected to be predominantly produced in the ejecta of SNe. To reveal what kind of dust grains form in the early universe, Todini & Ferrara (2001) calculated dust formation in primordial core-collapse supernovae (CCSNe), assuming uniform elemental composition and gas density within the He core. They have shown that the newly formed grains are amorphous carbon with size around 300 Å and Al_2O_3, $MgSiO_3$, Mg_2SiO_4, and Fe_3O_4 with size around 10–20 Å. By extending the model of dust formation by Todini & Ferrara (2001) to pair-instability supernovae (PISNe) whose progenitors evolve from metal-free stars with $M_{\rm pr} = 140{-}260\ M_\odot$ (Umeda & Nomoto 2002; Heger & Woosley 2002), Schneider et al. (2004) found that the typical sizes of dust formed in PISNe range from 0.001 to 0.3 μm depending on grain species. The dust models by Todini & Ferrara (2001) can successfully reproduce the extinction curve observed toward the BAL quasar SDSS 1048+46 at $z = 6.2$ (Maiolino et al. 2004b) and the IR spectral energy distribution (SED) of the blue compact dwarf galaxy SBS 0335−052 (Takeuchi et al. 2003) except for a slight overestimate of the far IR continuum; SBS 0335−052 is a good target in the local universe suitable for scrutinizing the properties of dust formed in SNe at high redshifts because of its young age ($<10^7$ yr) and low metallicity (1/41 $Z_\odot$; Vanzi et al. 2000).

However, as discussed by Kozasa et al. (1989), the species of dust formed in the ejecta largely depend on the elemental composition in the He core, and their sizes are affected by the time evolution of the gas density and temperature. Thus, Nozawa et al. (2003) extensively investigated dust production in Population III CCSNe and PISNe, by considering two extreme cases for the elemental composition in the ejecta: the unmixed case with the original onion-like structure and the uniformly mixed case within the He core. In the calculations of dust formation, the radial profile of the gas density is properly treated and the time evolution of the gas temperature is calculated by solving the radiative transfer equation including the energy deposition of radioactive elements, which are not taken into account by Todini & Ferrara (2001). Nozawa et al. (2003) found that a variety of grain species (C, Si, Fe, FeS, Al_2O_3, $MgSiO_3$, Mg_2SiO_4, SiO_2, and MgO) condense in the unmixed ejecta, reflecting the difference of the elemental composition at the formation site, and that only oxide and silicate grains (Al_2O_3, $MgSiO_3$, Mg_2SiO_4, SiO_2, and Fe_3O_4) form in the mixed ejecta with C/O $<$ 1. The average sizes of these grains span the range of 0.001−1 μm depending on the elemental composition and gas density at the location of formation in the ejecta. The species of dust formed in Population III SNe and the behaviors of their size distributions are almost independent of the progenitor mass, but the relative mass fraction of each grain species is dependent on it.

Based on the dust models by Nozawa et al. (2003), Hirashita et al. (2005) have shown that the extinction curve of the quasar SDSS 1048+46 at $z = 6.2$ can be better explained by the dust grains produced in the unmixed Population III CCSNe than those in the mixed Population III CCSNe. Takeuchi et al. (2005) have also shown by using the dust models for $M_{\rm pr} = 20\ M_\odot$ that only dust grains formed in the unmixed ejecta but not in the mixed ejecta can give an excellent fit to the observed SED of SBS 0335−052 over near- to far-IR wavelengths. These works strongly suggest that the comparisons with the observations relevant to dust in the early universe prefer dust grains produced in the unmixed Population III CCSNe rather than those in the mixed Population III CCSNe.

Therefore, as the representative model of the initial dust grains residing in the early ISM, we adopt the size distribution and abundance of each grain species obtained by the calculations of dust formation in the unmixed ejecta of a Population III SN with $M_{\rm pr} = 20\ M_\odot$ by Nozawa et al. (2003). For comparison, we also consider the model of dust formed in the mixed ejecta of the same SN. Hereafter, the models of dust formed in the unmixed and mixed ejecta are referred to as the unmixed grain model and the mixed grain model, respectively. The initial values of the depletion factor defined by the ratio of the total dust mass to the total metal mass produced in the SN are 0.224 for the unmixed grain model and 0.297 for the mixed grain model. The bulk density $\rho_{d,j}$, mass fraction A_j, and average size $a_{{\rm ave},j}$ of each grain species are summarized in Table 2, and their size spectra are given in Figure 6*a* for the unmixed grain model and in Figure 7*a* for the mixed grain model, where the bin width is 0.1 dex.

It is useful for the following discussion to address here the behavior of the size distribution of each dust species produced in the unmixed ejecta. C, Fe, and SiO_2 grains have a lognormal-like size distribution with the relatively large average radius of >0.01 μm, while the size distribution functions of FeS, Mg_2SiO_4, and MgO grains are approximately power law. The average radii of Al_2O_3 and $MgSiO_3$ grains are very small ($<5 \times 10^{-3}\ \mu$m). Note that the Si grain shows a bimodal size distribution: the grains with size less than 0.03 μm occupy almost 100% in number but only 0.2% in mass. Thus, as the average radius of the Si grain, we take

TABLE 2
DUST MODELS USED IN THE CALCULATIONS

		Unmixed Grain Model		Mixed Grain Model	
Dust Species	$\rho_{d,j}$ (g cm^{-3})	A_j	$a_{\mathrm{ave},j}$ (μm)	A_j	$a_{\mathrm{ave},j}$ (μm)
C	2.26	0.103	0.029	...	...
Si	2.32	0.304	0.250	...	...
Fe	7.89	0.050	0.148	...	...
FeS	4.84	0.156	0.0088	...	...
Al_2O_3	3.98	0.002	0.0007	0.001	0.0003
$MgSiO_3$	3.18	0.010	0.0045	0.102	0.011
Mg_2SiO_4	3.20	0.219	0.0066	0.205	0.010
SiO_2	2.64	0.100	0.047	0.588	0.033
MgO	3.56	0.056	0.0058	...	...
Fe_3O_4	5.21	...	...	0.103	0.0022

NOTES.—The models of dust grains are adopted from the results of the calculations of dust formation in the ejecta of a Population III SN with $M_{\mathrm{pr}} = 20\,M_\odot$ by Nozawa et al. (2003). The bulk density of grain species j is denoted by $\rho_{d,j}$. The mass fraction A_j and the average size $a_{\mathrm{ave},j}$ of each grain species are given for the unmixed and mixed grain models. Note that the average radius of Si grains in the unmixed grain model is calculated for the grains larger than 0.03 μm, which occupy 99.8% of the total mass.

0.25 μm calculated for the grains larger than 0.03 μm including 99.8% of the mass. The size distribution function summed up over all grain species is well fitted with a broken power-law formula whose index is -3.5 for the radius larger than 0.06 μm and -2.5 for the smaller one.

4. PHYSICS OF INTERSTELLAR SHOCK

The deceleration rate due to drag force and the erosion rate due to sputtering of dust grains depend on the time evolution of gas temperature and density in the postshock flow. In this section, we present the basic equations and initial conditions for the hydrodynamic calculation of the time evolution of the shock and the method of the simulation for dust destruction in the shock.

4.1. *The Basic Equations for the Gas Dynamics*

The hydrodynamic equations for gas to calculate the time evolution of a spherically symmetric interstellar shock driven by a SN explosion, using conventional physical variables, are given by

$$\frac{\partial \rho}{\partial t} + \frac{1}{r^2}\frac{\partial}{\partial r}(r^2 \rho v) = 0, \qquad (4)$$

$$\frac{\partial}{\partial t}(\rho v) + \frac{1}{r^2}\frac{\partial}{\partial r}(r^2 \rho v^2) = -\frac{\partial P}{\partial r}, \qquad (5)$$

$$\frac{\partial U}{\partial t} + \frac{1}{r^2}\frac{\partial}{\partial r}\left[r^2 (U + P) v\right] = -\Lambda(n_{\mathrm{H}}, T), \qquad (6)$$

where $P = \rho kT/\mu m_{\mathrm{H}}$ is the gas pressure with mean molecular weight μ and hydrogen mass m_{H}, and the sum of kinetic energy and thermal energy per unit volume is

$$U = \frac{1}{2}\rho v^2 + \frac{P}{\gamma - 1} \qquad (7)$$

with adiabatic index γ, and we adopt $\gamma = 5/3$ in the calculation.

The cooling rate of gas $\Lambda(n_{\mathrm{H}}, T)$ in units of ergs s^{-1} cm^{-3} is expressed by

$$\Lambda(n_{\mathrm{H}}, T) = n_e n_{\mathrm{H}} \Lambda_{\mathrm{gas}}(T) + \Lambda_{\mathrm{ic}}(T) + \Lambda_d(n_{\mathrm{H}}, T), \qquad (8)$$

where each term represents the rate of cooling by the atomic process, by inverse Compton scattering, and by the thermal emission of dust. In the calculations, we adopt the gas cooling function $\Lambda_{\mathrm{gas}}(T)$ for the zero metal case given in Sutherland & Dopita (1993) and ignore the contribution of cooling by metal ions ejected from dust by sputtering because, as mentioned in § 3.1, the metals do not contribute to the cooling of gas for a metallicity of $Z = 10^{-4}\,Z_\odot$ (Sutherland & Dopita 1993). For the inverse Compton scattering caused by collisions of hot electrons in the shock with CMB photons, the cooling rate $\Lambda_{\mathrm{ic}}(T)$ is given by (Ikeuchi & Ostriker 1986)

$$\Lambda_{\mathrm{ic}}(T) = 5.41 \times 10^{-32}(1 + z)^4 n_e T_4, \qquad (9)$$

where T_4 is the gas temperature in units of 10^4 K, and we take $z = 20$ in the calculation. The cooling function $\Lambda_d(n_{\mathrm{H}}, T)$ through the thermal emission from dust heated by collisions with gas particles in the shock is calculated by (Dwek 1987)

$$\Lambda_d(n_{\mathrm{H}}, T) = \sum_j n_{d,j} \int H_j(a, T, n_{\mathrm{H}}) f_j(a)\, da, \qquad (10)$$

where $n_{d,j}$ and $f_j(a)$ are, respectively, the number density and size distribution function of dust species j at a given t and r. The collisional heating rate $H_j(a, T, n_{\mathrm{H}})$ of grain species j is given in § 6.3.

The time evolution of gas temperature and density in a shock driven by a SN is characterized by the explosion energy E_{51} and the progenitor mass M_{pr}, which specify the structures of density and velocity of gas in the ejecta. Thus, as the initial condition for interstellar shocks, we adopt the hydrodynamic models of the ejecta of Population III SNe with various E_{51} and M_{pr} by Umeda & Nomoto (2002) to investigate the dependence of the efficiency of dust destruction on E_{51} and M_{pr}. Note that in the early universe with $Z = 10^{-4}\,Z_\odot$, the progenitors of SNe are not only Population III stars but also massive stars of the subsequent generation. However, the structures of density and velocity in a SN with a given E_{51} and M_{pr} do not depend very much on the initial metallicity of the progenitor star if its metallicity is less than $10^{-4}\,Z_\odot$ (H. Umeda 2002, private communication). In the calculations, we consider ordinary CCSNe with an explosion energy of $E_{51} = 1$, hypernovae (HNe) whose explosion energy is more than 10 times that of CCSNe, and PISNe whose progenitors are very massive ($M_{\mathrm{pr}} = 150$, 170, and 200 $M_\odot$); hereafter CCSNe and HNe with progenitor mass of $M_{\mathrm{pr}} = 13$–30 $M_\odot$ are referred to as Type II SNe (SNe II). The ejecta models used in the calculations are given in Table 3, where the labels C, H, and P represent CCSNe, HNe, and PISNe, respectively, and the numerical value denotes the mass of the progenitor in units of solar mass.

4.2. *The Method of the Simulations*

Equations (4)–(6) are solved by using the flux-splitting method with second-order accuracy in space and first-order accuracy in time (van Albada et al. 1982; Mair et al. 1988). This algorithm is one of the upwind schemes for the Euler equations and is well suited to solving problems involving a shock.

The calculations for the time evolution of the shock and dust destruction are performed via the following two steps. In the first step, we assume that the SN ejecta collides with the ISM in 10 yr after the explosion and calculate the time evolution of gas density and temperature without including dust, based on the ejecta models of Umeda & Nomoto (2002). The spatial mesh number is 500–5000 depending on the gas density in the ISM, and the

TABLE 3
Models of Supernova Ejecta

Model	Progenitor Mass ($M_\odot$)	Explosion Energy E_{51} (10^{51} ergs)
C13	13	1
C20	20	1
C25	25	1
C30	30	1
H25	25	10
H30	30	30
P150	150	1
P170	170	20
P200	200	28

Notes.—The models of the SN ejecta are adopted from Umeda & Nomoto (2002). In the model names, the labels C, H, and P represent CCSNe, HNe, and PISNe, respectively, and the numerical value denotes the mass of the progenitor in units of solar masses.

inner 20 mesh points are assigned to the ejecta. Note that dust destruction in this first step does not contribute to the evaluation of the destruction efficiency because the mass of gas swept up by the shock is less than 0.1% of that by $t = t_{\rm tr}$. In addition, the cooling of gas by dust has no effects on the subsequent structure of the shock. In the second step, fixing the spatial mesh number to 430, we rearrange the density, temperature, and velocity of the postshock gas obtained from the first step into the inner 30 linear mesh points. Then, including dust, we calculate the time evolution of the shock, as well as the dynamics and destruction of the dust.

By treating dust as a test particle, the physical processes relevant to dust are calculated as follows. Consider a stationary ($v_d = 0$) dust grain characterized by its composition and number density with radius between a and $a + da$ at a given position R_d in the ISM. Once the grain enters the shock front, the relative velocity to gas $w_d = v - v_d$ is assigned. Then for the temperature T and density $n_{\rm H}$ of gas at the shock front, we calculate the deceleration rate dw_d/dt due to drag force, the erosion rate da/dt by sputtering, and the heating rate $H(a, T, n_{\rm H})$ by collisions with gas. By updating the relative velocity by $w_d' = w_d + (dw_d/dt)\Delta t$ and the grain radius by $a' = a + (da/dt)\Delta t$ for a given small time step Δt, the velocity and position of the dust at time $t' = t + \Delta t$ are calculated by $v_d' = v + w_d'$ and $R_d' = R_d + v_d'\Delta t$. The procedure described above is repeated for the gas temperature T and density $n_{\rm H}$ at the position R_d' of the grain. Note that the dust grain is defined to be completely destroyed if the grain radius is smaller than the nominal monomer radius of condensate given in Nozawa et al. (2003).

5. EVALUATION OF SPUTTERING YIELD

Sputtering is divided into two categories reflecting the difference in the underlying mechanisms: physical sputtering and chemical sputtering. Physical sputtering invokes a transfer of kinetic energy from the incident particle to target atoms and subsequent ejection of those atoms that have acquired enough kinetic energy to overcome the binding forces exerted by the target. Chemical sputtering invokes a chemical reaction induced by the impinging particles that produces an unstable compound at the target surface (Sigmund 1981). In the high-velocity shocks considered in this paper, dust grains are predominantly destroyed by physical sputtering because the dust temperature is at most 100 K in the postshock region (Dwek 1987); chemical sputtering is of no importance, since this process occurs at a temperature as high as 800 K (Roth 1983). Thus, in what follows, we simply refer to physical sputtering as "sputtering." The efficiency of destruction by sputtering is characterized by the sputtering yield defined as the mean number of emitted atoms per incident particle. The sputtering yield depends on the impact energy of a projectile and the incident angle to the target surface, as well as on the projectile-target combination. However, only a few sets of experimental data on sputtering yield are available for the combinations of dust materials and ion species of interest to us.

One method of evaluating the sputtering yields for the projectile-target combinations of astrophysical interest is to apply the Monte Carlo code for the transport of ions in matter (TRIM; Ziegler et al. 1985) that simulates the energy loss of a projectile ion with given impact energy and incident angle in a solid (Field et al. 1997; May et al. 2000; Bianchi & Ferrara 2005). The TRIM code requires as input parameters not only the surface binding energy of the target but also the displacement energy E_d and the lattice binding energy E_b. Particularly, uncertainties in the value of E_d are a significant source of error in the calculated sputtering yield (May et al. 2000; Bianchi & Ferrara 2005). In fact, the sputtering yields computed by this simulation code have been known to significantly differ from the experimental data at low impact energies (Bianchi & Ferrara 2005). Furthermore, it is time consuming to combine the Monte Carlo simulation with the hydrodynamic calculation for dust destruction.

Another method is to apply the universal relation, which is the analytic formula derived by Bohdansky (1984) for the energy dependence of sputtering yield at normal incidence for a monatomic solid. To investigate the destruction of interstellar dust such as C, Fe, SiC, SiO_2, and H_2O ice, Tielens et al. (1994) have applied the universal relation by treating the constant K in this formula as a parameter, and they determined it by comparing the available experimental data with the sputtering yield calculated by the universal relation. They have shown that the universal relation can be applied to not only monatomic solids but also compound solids by taking the appropriate average values for the atomic and mass numbers and the surface binding energy under the assumption that each element comprising the target is sputtered off at the same rate. However, the agreement of the calculated sputtering yield with the experimental data is not very good for the ion-target combinations with a mass ratio of target atom to incident ion ranging from 0.7 to 2.

Therefore, we apply the universal relation for sputtering yield with a slight modification so as to reproduce the experimental data well, collecting and minutely examining a large amount of sputtering data, in order to evaluate the sputtering yields for the combinations of dust and ion species of interest to us. Following Tielens et al. (1994), we treat K as a free parameter and determine it by fitting to the experimental data for the grain species with the yield data covering a wide range of impact energy of the projectiles. For the grain species for which little or no sputtering data are available, we deduce the value of K by fitting to the sputtering yield calculated by means of the Monte Carlo code for the erosion and deposition based on a dynamic model (EDDY; Ohya & Kawata 1997). The EDDY code requires only the surface binding energy as an input parameter and allows us to predict the sputtering yield for a specific impact energy and incident angle more easily than the TRIM code, although the energy range applicable to the calculations is limited to 0.1–10 keV. In the following subsection, we first introduce the universal relation for sputtering yield and then determine the value of K for each grain species by fitting to the available experimental data and/or the results of the EDDY simulation.

5.1. *Universal Relation for Sputtering Yield*

For backward sputtering and with the neglect of inelastic energy losses, the sputtering yield at normal incidence $Y_i^0(E)$ by the projectile i impacting with energy E is given by (Bohdansky 1984)

$$Y_i^0(E) = 4.2\times 10^{14}\frac{S_i(E)}{U_0}\frac{\alpha_i(\mu_i)}{K\mu_i+1}\left[1-\left(\frac{E_{\rm th}}{E}\right)^{2/3}\right]\left(1-\frac{E_{\rm th}}{E}\right)^2, \quad (11)$$

where U_0 is the surface binding energy in units of eV, $\mu_i = M_d/M_i$ is the ratio of the mass number of the target atom to the incident ion, α_i is the energy-independent function of μ_i, and K is treated as a free parameter to be adjusted to reproduce the experimental data (Tielens et al. 1994). The threshold energies $E_{\rm th}$ have been obtained by fitting the yield data for low-energy sputtering and are approximately given by (Bohdansky et al. 1980; Andersen & Bay 1981)

$$E_{\rm th} = \begin{cases} \dfrac{U_0}{g_i(1-g_i)} & \text{for} \quad \dfrac{M_i}{M_d} \le 0.3, \\ 8U_0\left(\dfrac{M_i}{M_d}\right)^{1/3} & \text{for} \quad \dfrac{M_i}{M_d} > 0.3, \end{cases} \quad (12)$$

where $g_i = 4M_iM_d/(M_i+M_d)^2$ is the maximum fractional energy transfer possible in a head-on elastic collision. The function $S_i(E)$ is the nuclear stopping cross section in units of ergs cm^2 and can be expressed by the following universal relation (Sigmund 1981):

$$S_i(E) = 4\pi a_{\rm sc}Z_iZ_de^2\frac{M_i}{M_i+M_d}s_i(\epsilon_i), \quad (13)$$

where e is the elementary charge and Z_i and Z_d are the atomic numbers of the projectile and the target, respectively. The screening length $a_{\rm sc}$ for the interaction potential between the nuclei is given by

$$a_{\rm sc} = 0.885a_0\left(Z_i^{2/3}+Z_d^{2/3}\right)^{-1/2} \quad (14)$$

with the Bohr radius $a_0 = 0.529$ Å. The function $s_i(\epsilon_i)$ depends on the detailed form adopted for the screened Coulomb interaction and can be approximated by (Matsunami et al. 1980)

$$s_i(\epsilon_i) = \frac{3.441\sqrt{\epsilon_i}\ln(\epsilon_i+2.718)}{1+6.35\sqrt{\epsilon_i}+\epsilon_i\left(-1.708+6.882\sqrt{\epsilon_i}\right)}, \quad (15)$$

where the reduced energy ϵ_i is given by

$$\epsilon_i = \frac{M_d}{M_i+M_d}\frac{a_{\rm sc}}{Z_iZ_de^2}E. \quad (16)$$

The value of $\alpha_i(\mu_i)$ in equation (11) depends on how the distribution of energy deposited in the target is approximated. Sigmund (1969) suggested the three types of approximations according to the adopted distribution function (Gaussian, corrected Gaussian, and non-Gaussian). The values of $\alpha_i(\mu_i)$ obtained by these approximations are very similar (Sigmund 1969) and are approximately expressed for $\mu_i \le 10$ as follows (e.g., Bohdansky 1984):

$$\alpha_i = \begin{cases} 0.2 & \text{for} \quad \mu_i \le 0.5, \\ 0.3\mu_i^{2/3} & \text{for} \quad 0.5 < \mu_i \le 10. \end{cases} \quad (17)$$

TABLE 4
Parameters for Calculations of Sputtering Yield and References for Yield Data

Dust Species	U_0 (eV)	Z_d	M_d	K	References
C	4.0	6	12	0.61	1, 2, 3, 4, 5
Si	4.66	14	28	0.43	3, 4, 6, 7, 8, 9, 10, 11
Fe	4.31	26	56	0.23	3, 4, 5, 7, 8, 12, 13
FeS	4.12	21	44	0.18	EDDY
Al_2O_3	8.5	10	20.4	0.08	3, 14, 15
$MgSiO_3$	6.0	10	20	0.1	16
Mg_2SiO_4	5.8	10	20	0.1	16
SiO_2	6.42	10	20	0.1	3, 14, 15, 17, 18
MgO	5.17	10	20	0.06	14, 15, EDDY
Fe_3O_4	4.98	15.7	33.1	0.15	EDDY

Notes.—The surface binding energy is represented by U_0. The mean atomic number and mean mass number of the target material are Z_d and M_d, respectively, and the free parameter K is determined by fitting to the available experimental data and/or the results of the EDDY simulation. See text for details.

References.—(1) Bohdansky et al. 1978; (2) Bohdansky et al. 1976; (3) Roth et al. 1979; (4) Rosenberg & Wehner 1962; (5) Hechtl et al. 1981; (6) Laegreid & Wehner 1961; (7) Southern et al. 1963; (8) Eernisse 1971; (9) Sommerfeldt et al. 1972; (10) Coburn et al. 1977; (11) Blank & Wittmaack 1979; (12) von Seefeld et al. 1976; (13) Bohdansky et al. 1977; (14) Bach 1970; (15) Nenadovic et al. 1990; (16) Tielens et al. 1994; (17) Bach et al. 1974; (18) Edwin 1973.

However, equation (17) for α_i slightly overestimates the sputtering yields for the projectile-target combinations with a mass ratio of $0.7 \lesssim \mu_i \lesssim 2$. Hence, from a comparison with a large amount of sputtering data, we apply the following formula for α_i:

$$\alpha_i = \begin{cases} 0.2 & \text{for} \quad \mu_i \le 0.5, \\ 0.1\mu_i^{-1}+0.25(\mu_i-0.5)^2 & \text{for} \quad 0.5 < \mu_i \le 1, \\ 0.3(\mu_i-0.6)^{2/3} & \text{for} \quad 1 < \mu_i. \end{cases} \quad (18)$$

As we show below, this modified function α_i can produce excellent agreement with the sputtering data for any values of μ_i considered here ($0.3 \le \mu_i \le 56$).

By treating K as a parameter, the surface binding energy U_0 must be specified to evaluate the normal-incidence sputtering yield $Y_i^0(E)$ from equation (11). We assume U_0 to be equal to the sublimation energy and evaluate it from the JANAF Thermochemical Tables (Chase et al. 1985) except for C and Al_2O_3, whose values of U_0 are discussed below. The values of U_0 for each grain species are summarized in Table 4 along with the values of Z_d and M_d.

5.2. *Sputtering Yield of Each Grain Species*

In order to evaluate the sputtering yield for the projectile-target combinations of interest to us, we determine the value of K by fitting to the experimental data for C, Si, Fe, SiO_2, and Al_2O_3 grains for which a sufficient amount of sputtering data are available. For MgO, FeS, and Fe_3O_4 grains for which little or no yield data are available, we evaluate K by fitting to the results of the EDDY simulation. The experimental and simulated sputtering data at normal incidence, for which the references are summarized in Table 4, are given in Figure 1 along with the best-fitting theoretical yield calculated by the universal relation (*solid lines*). In Figures 1*a*–1*e*, the experimental data are shown for the following ion species: H^+ (*open circles*), D^+ (*asterisks*), He^+ (*open squares*), Ne^+ (*crosses*), and Ar^+ (*open triangles*). Even in the case that the

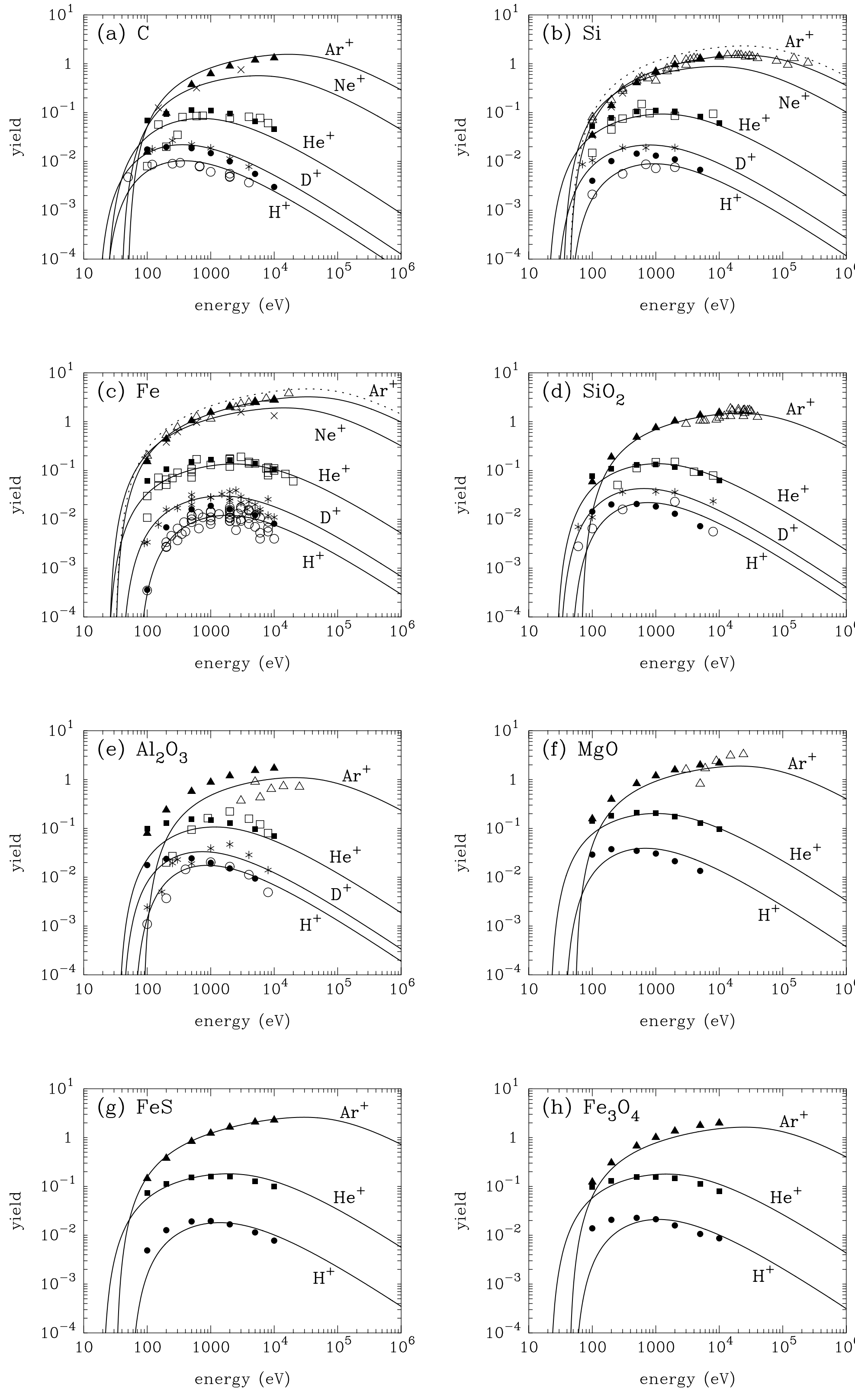

FIG. 1.—Sputtering yields of each grain species vs. incident energy of projectiles. (*a*) C, (*b*) Si, (*c*) Fe, (*d*) SiO_2, (*e*) Al_2O_3, (*f*) MgO, (*g*) FeS, and (*h*) Fe_3O_4. The incident ion species are H^+, D^+, He^+, Ne^+, and Ar^+. The experimental data on sputtering yield are represented by open circles (H^+), asterisks (D^+), open squares (He^+), crosses (Ne^+), and open triangles (Ar^+), and the results of the sputtering yield calculated by the EDDY code are denoted by filled circles (H^+), filled squares (He^+), and filled triangles (Ar^+). The solid curves show the best-fitting theoretical yields calculated by the universal relation. In (*b*) and (*c*), the dotted curves show the theoretical sputtering yields by Ar^+ projectile calculated by adopting α_i given by eq. (17). [*See the electronic edition of the Journal for a color version of this figure.*]

experimental data are sufficiently available, for comparison, we also plot the results of the EDDY calculations for the projectiles H^+ (*filled circles*), He^+ (*filled squares*), and Ar^+ (*filled triangles*).

As for C, the sublimation energy estimated to be $U_0 = 7.43$ eV from the thermodynamical data cannot reproduce the experimental data. Tielens et al. (1994) have shown that the ion fluences efficiently amorphize the surface layer of carbon material and reduce the surface binding energy. Thus, we take $U_0 = 4.0$ eV following Tielens et al. (1994), and this value gives a good fit to the measured yields with $K = 0.61$ (Fig. 1*a*) being different from $K = 0.65$ by Tielens et al. (1994); the difference stems from the adopted formula for α_i. The sputtering yield calculated by the EDDY code is enhanced for H^+ by a factor of 2–3 compared to the experimental data but gives a good agreement for He^+.

The sputtering data for the Si and Fe targets are sufficiently available. The modified universal relation employing equation (18) for α_i shows excellent agreement with the data points for all projectiles considered here (Figs. 1*b* and 1*c*), by adopting $K =$ 0.43 and 0.23, respectively. The EDDY calculations for Si and Fe targets also present good agreement with their measured data. The dotted lines indicate the sputtering yields by Ar^+ projectile calculated by using the values of K derived above but adopting α_i given by equation (17). It can be seen from these figures that equation (17) overestimates the sputtering yields for the projectile-target combinations with a mass ratio of $0.7 \lesssim \mu_i \lesssim 2$ as mentioned in § 5.1. It should be emphasized that the previous formula cannot reproduce the experimental data better than the modified universal relation whatever values of K are selected.

A very good fit of the universal relation to the experimental data is obtained for the SiO_2 target by taking $K = 0.1$ (Fig. 1*d*). This justifies the application of the universal relation to compound materials as shown by Tielens et al. (1994). The results of the EDDY simulations are consistent with the experimental data, but a comparison with the theoretical curves of sputtering yield shows a little enhancement for the H^+ and Ar^+ projectile at $E \leq$ 200 eV. For the $MgSiO_3$ and Mg_2SiO_4 materials for which sputtering data cannot be found in the literature, as in Tielens et al. (1994), we assume K to be 0.1, considering SiO_2 to be representative of silicates. In fact, this could be reasonable, since $K \simeq 0.1$ for the compounds including oxygen atoms (see Table 4).

Given the surface binding energy of $U_0 = 6.37$ eV evaluated from the thermodynamical data, the yield data of Al_2O_3 cannot be reproduced by the universal relation for any values of K. The disagreement of the theoretical prediction with the yield data is expected to be due to an unsuitable estimate of U_0, as is the case for C. Indeed, Roth et al. (1979) have suggested $U_0 = 8.5$ eV for Al_2O_3 from the behavior of the sputtering yield at impact energies below the maximum yield by He^+. Adopting this surface binding energy, we can get a better fit with $K = 0.08$ (Fig. 1*e*), although the agreement of the universal relation with the yield data is the worst among grain materials considered in this paper.

To our knowledge, little or no experimental data on sputtering yield exist for MgO, FeS, and Fe_3O_4. Thus, we employ the results by the EDDY calculations to extract the values of K for these materials. In Figures 1*f*–1*h* (1*f* for MgO, 1*g* for FeS, and 1*h* for Fe_3O_4), we show the EDDY results and the best-fitting theoretical curves. The agreement is not always good for H^+ and Ar^+ at low energies, which is also true for SiO_2, but the universal relation reproduces the yield data of SiO_2 well. Thus, we believe the fits to be reasonable and satisfactory for these materials. The values of K determined are 0.06, 0.18, and 0.15 for MgO, FeS, and Fe_3O_4, respectively.

Table 4 summarizes the value of K for each grain species evaluated by fitting to the available experimental data and/or the results of the EDDY simulations. We confirm that the derived value of K can well reproduce the experimental data of compounds, as well as single-element materials, by adopting appropriate average values for the atomic and mass numbers as proposed by Tielens et al. (1994). By slightly modifying the function $\alpha_i(\mu_i)$ in the universal relation, we realized that the calculated sputtering yields agree better with the available experimental data than before. The modified universal relation derived here could be applicable to evaluate the sputtering yield for any combinations of targets and projectiles of astrophysical interest as long as the experimental data are available.

6. PHYSICS OF DUST GRAINS IN SHOCK

The collisional interactions between dust and a hot gas in shock efficiently transfer charge, momentum, and energy between the two phases. As a result, dust grains acquire electric charge, undergo resistance to their motion through the gas, are eroded by sputtering, and are heated by collisions with gas. In addition, heated dust grains cool the gas through their thermal emission.

The electric charge on a grain plays an important role in grain physics in hot plasmas through the Coulomb interaction and the Lorentz force in the presence of magnetic field. Here we concentrate on the destruction of dust grains in fast ($\geq$100 km s^{-1}) and hot ($\geq$10^5 K) nonradiative shocks. For $T \gtrsim 10^6$ K, the effect of the electric charge of dust grains can be neglected because the dimensionless potential parameter ϕ defined by the ratio of the electric potential acquired by dust to the kinetic energy of gas is approximated by $\phi \sim 10^5/T$ and is significantly smaller than unity (Draine & Salpeter 1979; McKee et al. 1987). In addition, the erosion rate of refractory grains by thermal sputtering quickly decreases for $T < 10^6$ K (Draine & Salpeter 1979). Correspondingly, the erosion rate of dust grains by nonthermal sputtering decreases quickly for the relative velocity of dust to gas $w_d <$ 200 km s^{-1}. Therefore, it can be expected that the electric charge does not significantly affect the destruction of dust grains in the nonradiative shocks considered in this paper. Also, it is assumed that the early ISM is not pervaded by a magnetic field because the magnetic field in the early universe is considered to be very weak (Gnedin et al. 2000). Thus, we formulate the basic equations describing the motion of dust grains and their erosion by sputtering in postshock flow, neglecting the effect of charge on dust grains.

6.1. *Dynamics of Dust Grains*

Once dust grains that are at rest in the preshock ISM encounter the interstellar shock, they move ballistically behind the shock front with the initial velocity relative to gas $w_d \simeq \frac{3}{4} V_{\rm shock}$, where $V_{\rm shock}$ is the shock velocity, and are eroded by nonthermal sputtering. A grain streaming through the ionized gas is decelerated by a drag force due to the direct collisions with gas particles, and thus the velocity of dust relative to gas decreases. The drag force acting on a grain results from the momentum transfer from gas to dust. Under the assumption that a gas particle reflects specularly from the grain surface and that the kinetic temperature of gas is the same for all gas species, the deceleration rate of a spherical grain of radius a with velocity relative to gas w_d is given by (e.g., Draine & Salpeter 1979)

$$\frac{dw_d}{dt} = -\frac{3n_{\rm H}kT}{2a\rho_d}\sum_i A_i G_i(s_i), \tag{19}$$

where $n_{\rm H}$ is the number density of hydrogen atoms, k is the Boltzmann constant, T is the gas temperature, ρ_d is the bulk density of the grains, and $s_i^2 = m_i w_d^2/2kT$, with m_i being the mass of gas species i. The summation is taken over all gas species, and A_i is the number abundance of gas species i relative to that of hydrogen atoms. For the function $G_i(s_i)$, whose exact formula is given by Baines et al. (1965), the following analytical approximation has been proposed by Draine & Salpeter (1979):

$$G_i(s_i) \approx \frac{8s_i}{3\sqrt{\pi}}\left(1+\frac{9\pi}{64}s_i^2\right)^{1/2}, \tag{20}$$

with the accuracy within 1% for $0 < s_i < \infty$. In the calculations, we adopt this formula. It can be seen from equation (19) that grains with smaller size and/or higher relative velocity can be effectively decelerated by drag force and come to comove with gas in a shock.

6.2. *Grain Destruction by Sputtering*

The destruction of dust grains in high-velocity and high-temperature nonradiative shocks is dominated by sputtering. Actually, we can neglect the thermal evaporation of dust because the temperature of dust cannot rise as high as its sublimation temperature (~1000–2000 K) for the preshock gas density considered in this paper (e.g., Dwek 1987). Furthermore, we neglect the shattering process and partial vaporization caused by grain-grain collisions, since the number density of dust particles is very small in postshock flow and collisions between dust grains are extremely rare without a magnetic field.

The erosion rate of grains by sputtering is calculated by taking the angle-averaged sputtering yield $\langle Y_i(E_i)\rangle_\theta = 2Y_i^0(E_i)$ (Draine & Salpeter 1979) and is given by (e.g., Dwek et al. 1996)

$$\frac{da}{dt} = -\frac{m_{\rm sp}}{2\rho_d} n_{\rm H} \sum_i A_i \left(\frac{8kT}{\pi m_i}\right)^{1/2} \frac{e^{-s_i^2}}{2s_i} \times \int \sqrt{\epsilon_i} e^{-\epsilon_i} \sinh(2s_i\sqrt{\epsilon_i}) Y_i^0(\epsilon_i)\, d\epsilon_i, \tag{21}$$

where $\epsilon_i = E_i/kT$ and $m_{\rm sp}$ is the average mass of the sputtered atoms. Equation (21) can be reduced to the following equations for the two extreme cases of s_i (Dwek & Arendt 1992; Tielens et al. 1994): One is for $s_i \ll 1$, where a stationary grain suffers the thermal sputtering caused by collisions originating from the thermal motion of gas, and the erosion rate is written as

$$\frac{1}{n_{\rm H}}\frac{da}{dt} = -\frac{m_{\rm sp}}{2\rho_d}\sum_i A_i\left(\frac{8kT}{\pi m_i}\right)^{1/2}\int \epsilon_i e^{-\epsilon_i} Y_i^0(\epsilon_i)\, d\epsilon_i. \tag{22}$$

The other is in the limit of $s_i \to \infty$, where the nonthermal sputtering erodes a hypersonic grain with the rate given by

$$\frac{1}{n_{\rm H}}\frac{da}{dt} = -\frac{m_{\rm sp}}{2\rho_d} w_d \sum_i A_i Y_i^0(E = 0.5 m_i w_d^2). \tag{23}$$

Figure 2 shows the erosion rate of each dust species by sputtering in a gas with the primordial elemental composition of metallicity $Z = 10^{-4}\, Z_\odot$ given in Table 1; Figure 2*a* shows thermal sputtering versus the gas temperature T from equation (22), and Figure 2*b* shows nonthermal sputtering versus the velocity of dust relative to gas w_d from equation (23). The erosion rate by thermal (nonthermal) sputtering steeply increases from $T \sim 10^5$ K ($w_d \sim 30$ km s^{-1}), reaches a peak at $T = (4\text{–}20) \times 10^7$ K ($w_d = 500$–1300 km s^{-1}), and then slowly decreases with increasing T (w_d). This behavior of the erosion rate as a function of T and w_d reflects the dependence of sputtering yield on impact energy (see § 5.2). Among dust species considered in this paper, C grains have the lowest erosion rate at $T \geq 2 \times 10^6$ K ($w_d \geq 200$ km s^{-1}), which is about 1 order of magnitude lower than that of FeS grains with the highest rate at $T \geq 10^7$ K ($w_d \geq 400$ km s^{-1}). For thermal sputtering, the erosion rate da/dt for the other dust species is $\sim 1.2 \times 10^{-6} n_{\rm H}$ μm yr^{-1} cm^3 within a factor of 3 at $T \geq 2 \times 10^6$ K. For nonthermal sputtering at $w_d \leq 200$ km s^{-1}, the destruction by He$^+$ is dominant, and the erosion rate of Al_2O_3 is the lowest.

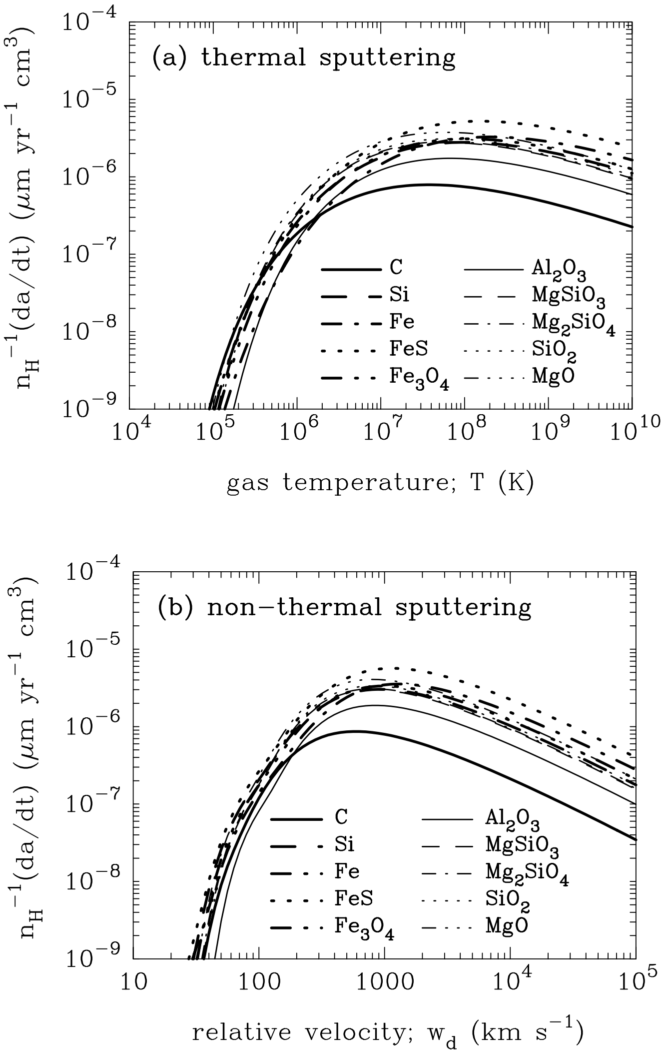

FIG. 2.—Erosion rate of each dust species by sputtering in units of μm yr^{-1} cm^3 calculated for the elemental composition of gas with $Z = 10^{-4}\, Z_\odot$ given in Table 1. (*a*) Thermal sputtering calculated by eq. (22) as a function of gas temperature T; (*b*) nonthermal sputtering calculated by eq. (23) as a function of velocity of dust relative to gas w_d. [*See the electronic edition of the Journal for a color version of this figure.*]

6.3. *Grain Heating*

The collisions with gas can also heat dust grains in postshock flow. The collisional heating rate $H(a, T, n_{\rm H})$ of a dust grain with radius a is presented by Dwek & Arendt (1992) as

$$H(a, T, n_{\rm H}) = n_{\rm H}\pi a^2 kT \sum_i A_i \left(\frac{8kT}{\pi m_i}\right)^{1/2}\frac{e^{-s_i^2}}{2s_i} \times \int \epsilon_i^{3/2} e^{-\epsilon_i}\sinh(2s_i\sqrt{\epsilon_i})\eta_i(a, \epsilon_i)\, d\epsilon_i, \tag{24}$$

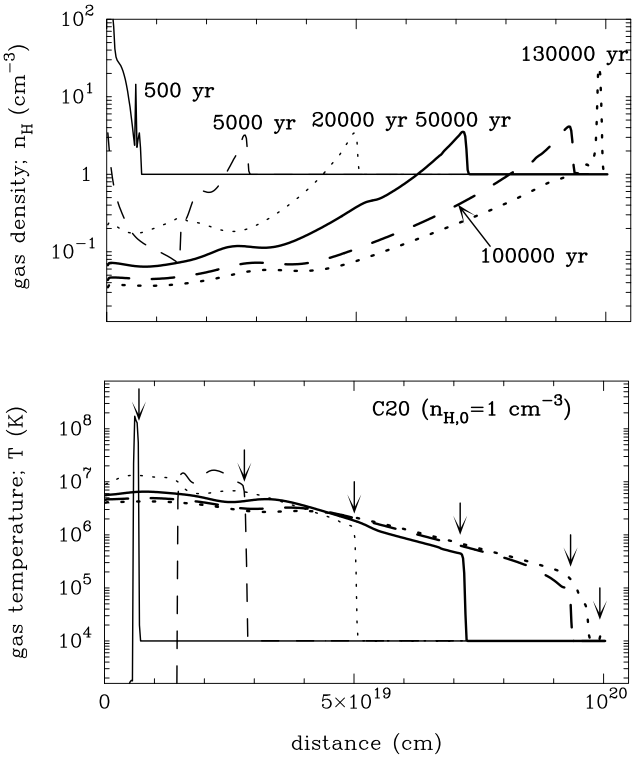

FIG. 3.—Structures of density (*top*) and temperature of gas (*bottom*) at given times in the interstellar shock that is driven by the SN model of C20 with $E_{51} = 1$ and $M_{\rm pr} = 20\ M_\odot$ and is propagating into the ISM with $n_{\rm H,0} = 1\ {\rm cm}^{-3}$. The arrow in the bottom panel indicates the position of the shock front at a given time. [*See the electronic edition of the Journal for a color version of this figure.*]

where $\eta_i(a, \epsilon_i)$ is the fraction of kinetic energy of gas species i deposited into the dust grain. The values of $\eta_i(a, \epsilon_i)$ are calculated by comparing the effective grain thickness $a_{\rm eff}$ ($4a/3$ for a spherical grain) with the stopping range of the incident particle l_s. When $a_{\rm eff} \geq l_s$, the incident particle deposits almost all of the energy into dust grains; otherwise, the difference between $a_{\rm eff}$ and l_s is exploited to determine the fraction of deposited energy. The approximations for the stopping range of ion species considered here are given in Dwek (1987). For the electron stopping range, we adopt the approximation derived by Tabata et al. (1972) and Iskef et al. (1983). This electron stopping range reduces the heating rate by $\sim$30% at $10^6\ {\rm K} \lesssim T \lesssim 10^9$ K compared with that given by Dwek (1987). The values and detailed derivation of $\eta_i(a, E)$ will be presented elsewhere (T. Nozawa et al. 2006, in preparation).

7. RESULTS OF CALCULATION OF DUST DESTRUCTION

In this section, we show the results of numerical simulations for dust destruction in a nonradiative shock, focusing on the results calculated for the ISM dust specified by the unmixed grain model described in § 3. In § 7.1, we demonstrate the time evolution of the temperature and density of the gas and the destruction of dust grains in the interstellar shock that is driven by the SN model of C20 with $E_{51} = 1$ and $M_{\rm pr} = 20\ M_\odot$ and is propagating into the ISM with $n_{\rm H,0} = 1\ {\rm cm}^{-3}$. In § 7.2, we investigate the dependences of the destruction efficiency and the mass of the gas swept up by the shock on E_{51}, $M_{\rm pr}$, and $n_{\rm H,0}$ and derive an approximation formula for the timescale of destruction for each dust species in the early universe. The effects of the cooling processes of gas on the evolution of the nonradiative shock and the destruction of dust are discussed briefly in § 7.3.

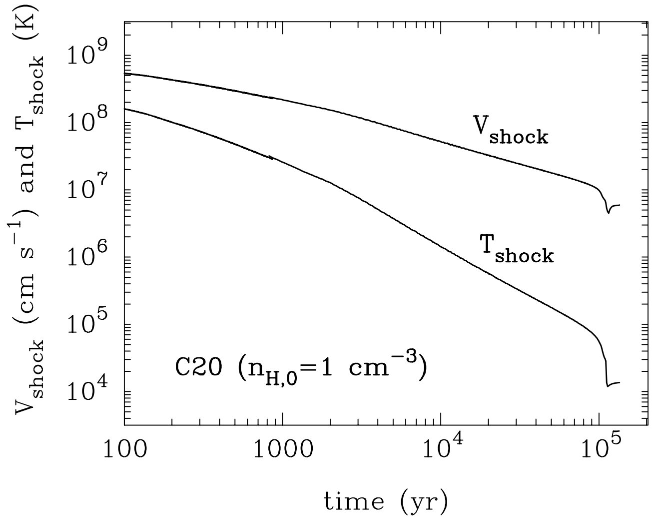

FIG. 4.—Time evolution of shock velocity $V_{\rm shock}$ and gas temperature $T_{\rm shock}$ at the shock front for model C20 with $n_{\rm H,0} = 1\ {\rm cm}^{-3}$. [*See the electronic edition of the Journal for a color version of this figure.*]

7.1. *Dust Destruction in Interstellar Shock for C20 Model*

7.1.1. *Time Evolution of Temperature and Density of Gas in Shock*

Figure 3 shows the structures of density (*top*) and temperature of gas (*bottom*) in a nonradiative shock at given times, and the solid lines in Figure 4 give the time evolution of the shock velocity $V_{\rm shock}$ and the gas temperature $T_{\rm shock}$ at the shock front. As shown in Figure 3, the gas density increases to 4 times that in the ISM and the gas temperature rises steeply at the shock front, which is indicated by the arrow for a given time step. With the initial shock velocity $\simeq$6000 km s^{-1}, the gas temperature at the shock front remains above 10^8 K until $t \simeq 200$ yr, and both $V_{\rm shock}$ and $T_{\rm shock}$ decrease with time. At $t > 5 \times 10^4$ yr after the explosion, the density of the gas in the inner postshock region is $\sim$1 order of magnitude lower than that in the unshocked region, and a low-density hot bubble with a temperature of several times 10^6 K is formed (Fig. 3). In this model, $V_{\rm shock}$ decelerates below 100 km s^{-1} at $t_{\rm tr} \simeq 10^5$ yr when the shock front travels the distance of $\simeq$30 pc and $T_{\rm shock}$ drops to several times 10^4 K. After that, a dense thin shell forms at the shock front because of the effective line cooling, and the supernova remnant (SNR) enters the radiative phase.

7.1.2. *Dynamics and Destruction of Dust Grains in Shock*

The motion of dust grains (Fig. 5, *top*) and the evolution of their sizes (Fig. 5, *bottom*) in postshock flow as a function of time are depicted in Figure 5, for example, for C grains with the initial size of 0.01 μm (*dashed line*), 0.1 μm (*dotted line*), and 1 μm (*thin solid line*). The thick solid curve (Fig. 5, *top*) indicates the position of the shock front. As dust grains initially at rest in the ISM intrude into the blast wave, they display different trajectories depending on their initial sizes, which clearly demonstrates that the dust grains are segregated and subjected to different sputtering processes in the postshock flow; small grains with initial radius of 0.01 μm are quickly decelerated by drag force, trapped in gas near the shock front, and completely destroyed by thermal sputtering. The 0.1 μm–sized grains are gradually decelerated to comove with gas in 7×10^3 yr after entering the shock. Large-sized grains with radius of 1 μm do not undergo as much deceleration by drag force and continue to keep a high velocity relative to gas. As a result, they are subjected to nonthermal sputtering, but their sizes are reduced very little, partly because they stay in the

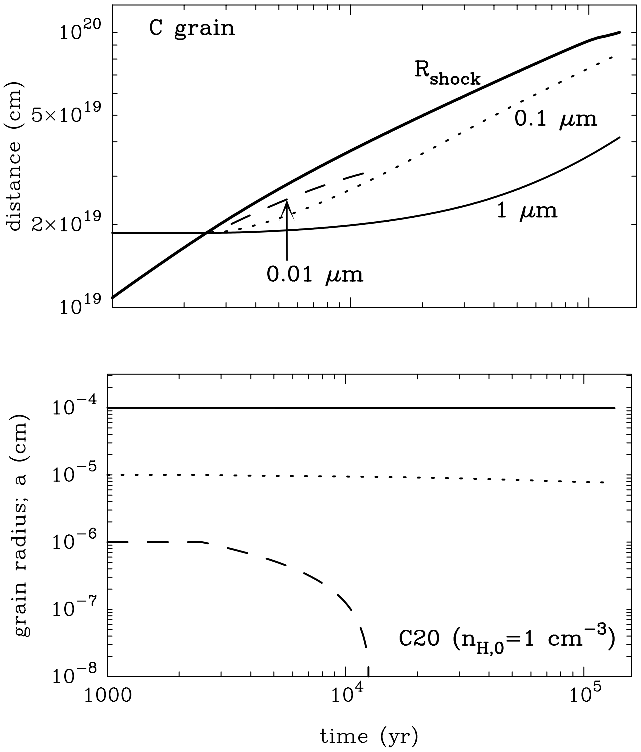

FIG. 5.—Time evolution of position (*top*) and size (*bottom*) of dust grains in postshock flow for model C20 with $n_{H,0} = 1$ cm^{-3}. The dust species considered is a C grain with size of 0.01 μm (*dashed line*), 0.1 μm (*dotted line*), and 1 μm (*thin solid line*). The thick solid curve in the top panel denotes the position of the shock front R_{shock}. [*See the electronic edition of the Journal for a color version of this figure.*]

inner region of the postshock flow where the gas density is lower than that near the shock front (see Fig. 3).

The modification of the size distribution of each dust species due to destruction by sputtering is illustrated in Figure 6: Figure 6*a* for the initial size distribution before destruction and Figure 6*b* for the size distribution after destruction. Since the erosion rate by sputtering does not strongly depend on grain size (see § 6.2), small grains are predominantly destroyed regardless of grain species; the number of small-sized grains such as Al_2O_3 is greatly reduced. C, SiO_2, and Fe grains whose initial size distributions are lognormal with a relatively large average size are eroded but not completely destroyed, and the numbers of smaller ones increase. Grains of size larger than 0.1 μm are little affected by erosion. Note that the size distribution summed up over all grain species gets flatter for the smaller radius with time compared with the corresponding initial size distribution approximated by a power-law formula with index of -2.5, while that for the larger radius remains almost unchanged.

7.1.3. *Efficiency of Dust Destruction*

The destruction efficiency ϵ_j of each grain species is given in Table 5 (see unmixed grain model) along with the initial average radius. The efficiency of dust destruction is expected to be higher for grain species with a smaller average size because the smaller grains are predominantly destroyed by sputtering. In fact, the efficiency of destruction of Al_2O_3 grains with the smallest average radius is 0.667 and is the highest among the dust species considered here. Si and Fe grains with initial average radii larger than 0.1 μm have destruction efficiencies of less than 0.2; 0.13 for Si grains and 0.15 for Fe grains. However, the destruction efficiency of C grains with the smaller average radius is smaller than that of SiO_2 grains because of the lowest erosion rate among all grain species at $T \gtrsim 2 \times 10^6$ K (see Fig. 2). In addition, FeS grains have a higher destruction efficiency (0.578) than those of Mg_2SiO_4 (0.451) and MgO grains (0.505) despite the larger initial average radius, which reflects not only the higher

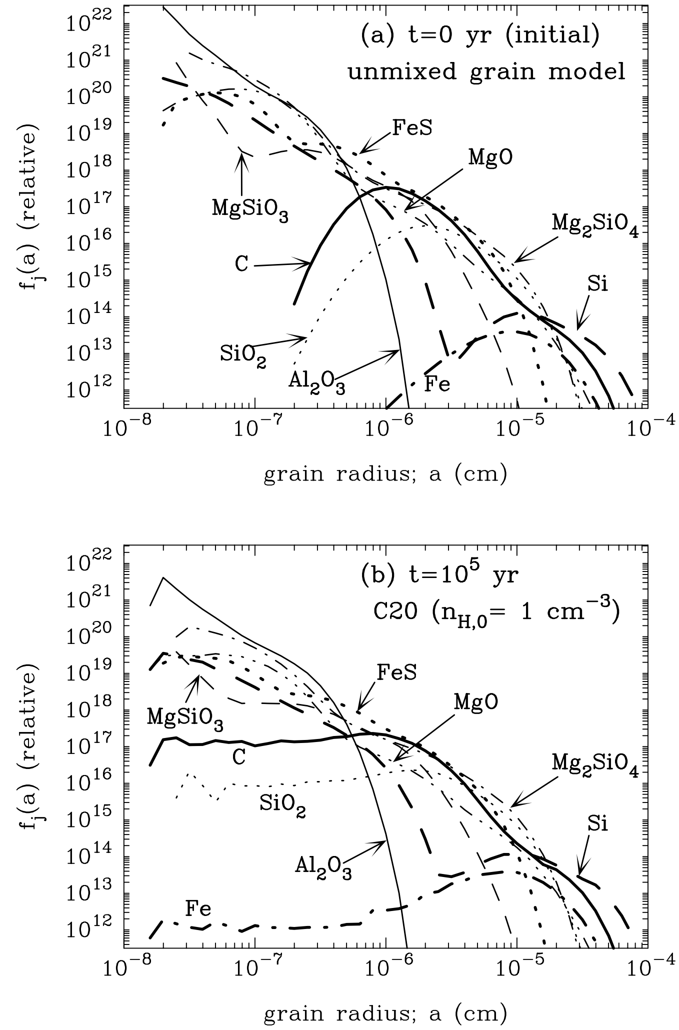

FIG. 6.—Size distribution of each dust species for the unmixed grain model for (*a*) the initial size distribution before destruction and (*b*) the size distribution obtained by the calculation of dust destruction for model C20 with $n_{H,0} = 1$ cm^{-3}. [*See the electronic edition of the Journal for a color version of this figure.*]

TABLE 5
THE EFFICIENCY OF DUST DESTRUCTION FOR C20 MODEL WITH $n_{H,0} = 1$

	UNMIXED GRAIN MODEL		MIXED GRAIN MODEL	
DUST SPECIES	ϵ_j	$a_{ave,j}$ (μm)	ϵ_j	$a_{ave,j}$ (μm)
C	0.247	0.029	...	...
Si	0.134	0.250	...	...
Fe	0.154	0.148	...	...
FeS	0.578	0.0088	...	...
Al_2O_3	0.667	0.0007	0.794	0.0003
$MgSiO_3$	0.637	0.0045	0.631	0.011
Mg_2SiO_4	0.451	0.0066	0.586	0.010
SiO_2	0.411	0.047	0.399	0.033
MgO	0.505	0.0058	...	...
Fe_3O_4	...	...	0.741	0.0022
Overall	0.340	...	0.497	...

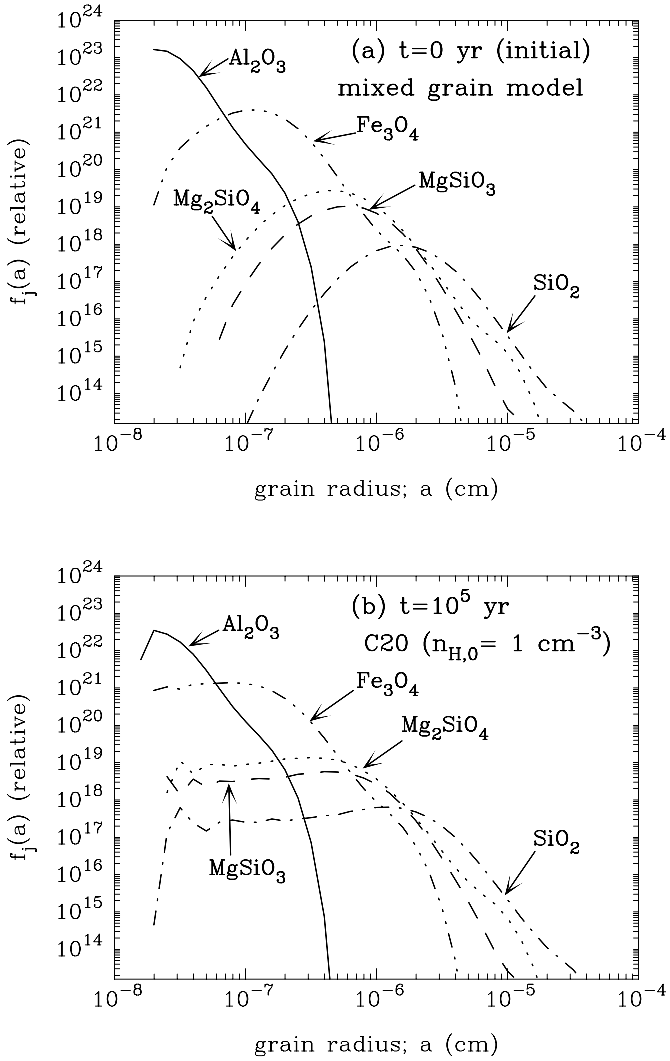

Fig. 7.—Same as Fig. 6, but for the mixed grain model. [*See the electronic edition of the Journal for a color version of this figure.*]

erosion rate at $T \gtrsim 10^7$ K but also a mass distribution that is much more weighted toward the smaller grains. Likewise, the destruction efficiency of $MgSiO_3$ grains with average size comparable to that of Mg_2SiO_4 and MgO is high (0.637) because of the lack of large grains. These facts indicate that the efficiency of dust destruction depends on the initial size distribution of dust grains, as well as on the sputtering yield.

In order to clarify the effect of the initial size distribution on the efficiency of dust destruction, we present the results of dust destruction for the mixed grain model calculated with the same SN model and value of $n_{H,0}$ as those for the unmixed grain model. Figure 7 shows the size distribution of each grain species (Al_2O_3, $MgSiO_3$, Mg_2SiO_4, SiO_2, and Fe_3O_4) before destruction (Fig. 7*a*) and after destruction (Fig. 7*b*), and the destruction efficiencies of these grains are tabulated in Table 5 (see mixed grain model). As is also the case for the unmixed grain model, the numbers of Al_2O_3 and Fe_3O_4 grains with the small average size (less than a few tens of angstroms) are considerably reduced, which results in high efficiencies of destruction (>0.7). For $MgSiO_3$, Mg_2SiO_4, and SiO_2 grains with lognormal size distributions, the erosion of large grains leads to an increase in the number of smaller ones, and their destruction efficiencies span the range of $0.4 \lesssim \epsilon_j \lesssim 0.64$. Note that although the average size is twice that in the unmixed case, the destruction efficiency (0.59) of Mg_2SiO_4 grains in the mixed case is significantly larger than that (0.45) in the unmixed case. The reason is that Mg_2SiO_4 grains formed in the unmixed ejecta have a power-law–like size distribution and include the large-sized grains of >0.1 μm that are barely destroyed in the shock; the average size is not always suitable for assessing the feasibility of dust destruction. Thus, we conclude that the dust destruction efficiency is very sensitive to the initial size distribution. The mass fraction of dust destroyed reaches up to 34% for the unmixed grain model and 50% for the mixed grain model.

7.2. *Timescale of Dust Destruction in the Early Universe*

In this subsection, we investigate the dependences of the efficiency of dust destruction ϵ_j and the mass of the gas swept up by the shock $M_{\rm swept}$ on E_{51}, $M_{\rm pr}$, and $n_{H,0}$ and derive an analytic formula describing the timescale of dust destruction for the unmixed grain model. Figure 8 shows the destruction efficiency of each grain species versus SN explosion energy calculated for $n_{H,0} = 1$ cm^{-3}; Figure 8*a* is for Al_2O_3, FeS, Mg_2SiO_4, and Fe grains, and Figure 8*b* is for $MgSiO_3$, MgO, SiO_2, C, and Si grains. In addition, the overall efficiency of dust destruction, which is defined as the ratio of the total mass of dust destroyed to the total mass of dust swept up by the shock, is plotted in Figure 8*a*. The SN models used for the calculations are distinguished by open circles (CCSNe), open squares (HNe), and filled triangles (PISNe).

The destruction efficiencies for each grain species are almost the same for CCSNe and a PISN with an explosion energy of $E_{51} = 1$ irrespective of the progenitor mass $M_{\rm pr}$, and they increase with increasing E_{51}. Note that a high explosion energy with $E_{51} \geq 10$ causes the temperature of the gas in the postshock flow to rise as high as 10^9 K, but this does not directly influence the efficiency of dust destruction because the increase of gas temperature does not always lead to the enhancement of the erosion rate by sputtering (see Fig. 2*a*). The reason for the increased efficiency with increasing E_{51} is considered as follows. The high-velocity shock (initial shock velocity $\gtrsim 10^4$ km s^{-1}) generated by the energetic SN explosion induces a high velocity of dust relative to gas. Then dust grains are efficiently decelerated by drag force (see eq. [19]), trapped in the high-density region near the shock front, and significantly eroded by thermal sputtering. Furthermore, since the high shock velocity takes a much longer time to drop down to 100 km s^{-1} (see Fig. 9), dust grains are immersed in a hot plasma for a long time, which causes even larger grains to be more eroded.

It should be pointed out here that the efficiencies of destruction for the models of P170 with $E_{51} = 20$ and P200 with $E_{51} = 28$ are a little higher than that for H30 with $E_{51} = 30$. The reason is that the ejecta mass of PISNe is more than 6 times larger than that of HNe, and the resulting longer duration of the free expansion phase causes the longer truncation time than that for HNe (Fig. 9). On the other hand, the efficiency of destruction for P150 with $M_{\rm pr} = 150$ $M_\odot$ and $E_{51} = 1$ is almost the same as that for CCSNe with $E_{51} = 1$ because the initial shock velocity ($\sim$3000 km s^{-1}) much lower than that of CCSNe makes the truncation time comparable to that of CCSNe. Therefore, although the destruction efficiency ϵ_j is almost independent of $M_{\rm pr}$ as long as $E_{51} = 1$, the ϵ_j for PISNe higher than that for HNe at $E_{51} \geq 10$ reflects the difference in the explosion mechanism depending on the progenitor mass.

To examine the dependence of ϵ_j on E_{51} for each type of SN, we calculate the coefficients $a_{1,j}$ and $b_{1,j}$ in equation (A1) given in the Appendix for SNe II (C13, C20, C25, C30, H25, and H30) and PISNe (P150, P170, and P200) separately, and the calculated overall efficiencies of dust destruction are indicated by dotted

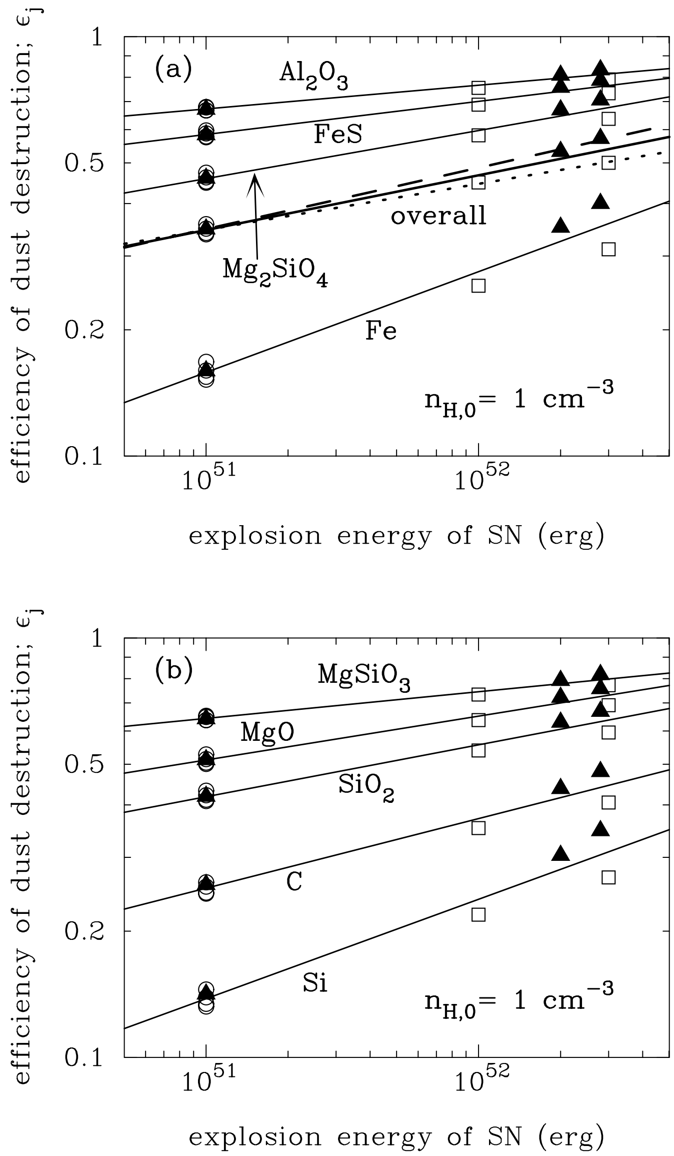

Fig. 8.—Efficiency of destruction of each grain species in the unmixed grain model calculated for $n_{H,0} = 1$ cm^{-3} as a function of SN explosion energy for (*a*) Al_2O_3, FeS, Mg_2SiO_4, and Fe grains and (*b*) $MgSiO_3$, MgO, SiO_2, C, and Si grains. The SN models used for the calculations are distinguished by open circles (CCSNe), open squares (HNe), and filled triangles (PISNe). In (*a*), the overall efficiency of dust destruction is also plotted. The linear solid lines for each grain species are the results calculated by the power-law formula given by eq. (A1) for all SNe. The dotted and dashed lines for the overall efficiencies of dust destruction are the results of calculations for SNe II and for PISNe, respectively. [*See the electronic edition of the Journal for a color version of this figure.*]

(SNe II) and dashed lines (PISNe) in Figure 8*a*. Although the difference in the efficiency of dust destruction between SNe II and PISNe increases with increasing E_{51}, the deviations from the values calculated by $a_{1,j}$ and $b_{1,j}$ for all SN models are at most about 10% at $E_{51} = 30$. Thus, we consider ϵ_j to be almost independent of M_{pr} as long as E_{51} is the same. For reference, we tabulate the values of $a_{1,j}$ and $b_{1,j}$ for SNe II and PISNe in Table 6. The mass of gas swept up by shock M_{swept} and the truncation time t_{tr} calculated for $n_{H,0} = 1$ cm^{-3} are presented in Figure 9 as a function of SN explosion energy. As is also the case for ϵ_j, M_{swept} and t_{tr} are almost the same for $E_{51} = 1$ regardless of M_{pr}, and they increase with increasing E_{51}.

Next, we show the dependences of ϵ_j and M_{swept} on the preshock gas density $n_{H,0}$. Figure 10*a* plots the overall efficiency of

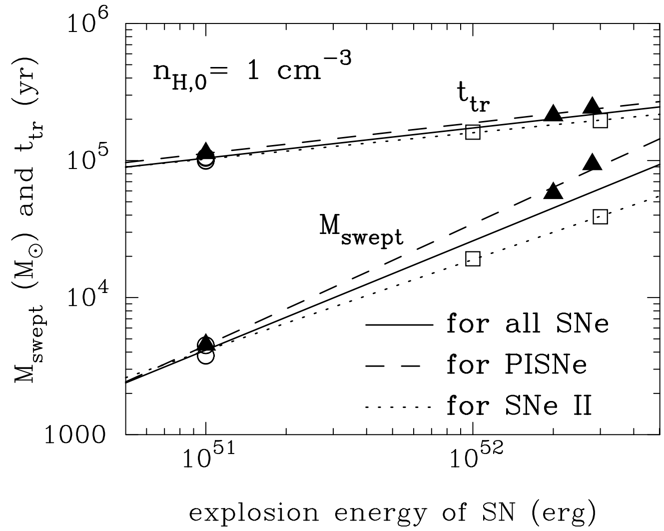

Fig. 9.—Mass of gas swept up by shock, M_{swept}, and truncation time t_{tr} vs. explosion energy of SNe for $n_{H,0} = 1$ cm^{-3}. The results for CCSNe, HNe, and PISNe are represented by open circles, open squares, and filled triangles, respectively. The linear lines are the power-law formula approximated by eq. (A2) for all SNe (*solid lines*), SNe II (*dotted lines*), and PISNe (*dashed lines*). [*See the electronic edition of the Journal for a color version of this figure.*]

dust destruction versus $n_{H,0}$ for C20 (*crosses*), H25 (*open circles*), and H30 models (*filled triangles*) with $E_{51} = 1$, 10, and 30, respectively. The efficiency of dust destruction increases with increasing $n_{H,0}$, since higher gas density causes more frequent collisions between dust and gas to efficiently erode the surface of dust grains by sputtering; for example, the mass fraction of dust destroyed for the H30 model is 78% for $n_{H,0} = 10$ cm^{-3} but only 23% for $n_{H,0} = 0.1$ cm^{-3}. In Figure 10*b*, we present the mass of the gas swept up by the shock M_{swept} as a function of $n_{H,0}$ for the C20, H25, and H30 models. Note that M_{swept} decreases with increasing $n_{H,0}$ because the shock wave more quickly decelerates and travels only a small distance.

The approximation formulae presented in the Appendix being combined, the timescale of destruction for each dust species by the interstellar shock in the early universe is presented by

$$\tau_{SN,j}^{-1} = \epsilon_j(E_{51}, n_{H,0}) \frac{4144 E_{51}^{0.8} n_{H,0}^{-0.142 E_{51}^{0.063}} M_\odot}{M_{ISM}} \gamma_{SN} \qquad (25)$$

for all SN models, where the dependences of ϵ_j on E_{51} and $n_{H,0}$ are given by equations (A1) and (A3), respectively. We derived the timescale of dust destruction as a function of not only the explosion energy of SNe but also the gas density in the ISM. The swept-up gas mass is proportional not to E_{51} but to $\sim E_{51}^{0.8}$, being different from the formula proposed by McKee (1989). The timescale of dust destruction derived here could be applicable to investigating the time evolution of dust grains in the early universe. In particular, the difference of the efficiency of dust destruction for each grain species may have a great influence on the amount and size distribution of dust grains residing in early interstellar space.

7.3. *The Effects of the Cooling Processes of Gas on Dust Destruction*

Figure 11 shows the cumulative energy lost by the atomic process (*dashed line*), the inverse Compton scattering (*dotted line*), and the thermal emission from dust (*thin solid line*) calculated for the SN model of C20 and for the ISM with parameters of

TABLE 6
COEFFICIENTS FOR ϵ_j OF THE APPROXIMATION FORMULA (A1)

	For All SNe		For SNe II		For PISNe	
Dust Species	$a_{1,j}$	$b_{1,j}$	$a_{1,j}$	$b_{1,j}$	$a_{1,j}$	$b_{1,j}$
C	2.532E−01	1.660E−01	2.526E−01	1.407E−01	2.580E−01	1.820E−01
Si	1.380E−01	2.371E−01	1.377E−01	1.979E−01	1.414E−01	2.631E−01
Fe	1.583E−01	2.402E−01	1.586E−01	2.005E−01	1.594E−01	2.707E−01
FeS	5.842E−01	7.897E−02	5.850E−01	6.758E−02	5.834E−01	8.857E−02
Al_2O_3	6.724E−01	5.649E−02	6.733E−01	4.803E−02	6.709E−01	6.393E−02
$MgSiO_3$	6.429E−01	6.358E−02	6.438E−01	5.421E−02	6.417E−01	7.165E−02
Mg_2SiO_4	4.585E−01	1.146E−01	4.590E−01	9.827E−02	4.595E−01	1.275E−01
SiO_2	4.183E−01	1.238E−01	4.189E−01	1.054E−01	4.190E−01	1.383E−01
MgO	5.117E−01	1.046E−01	5.122E−01	9.020E−02	5.124E−01	1.160E−01
Overall	3.458E−01	1.307E−01	3.460E−01	1.099E−01	3.476E−01	1.463E−01

$n_{\rm H,0} = 1$ and $Z = 10^{-4}\,Z_\odot$ at a redshift of $z = 20$. The total energy lost by these cooling processes is drawn by the thick solid curve. The inverse Compton cooling is comparable to that by the atomic process in the early phase of the SNR ($t < 10^4$ yr). As the gas temperature decreases, the atomic process by H and He line cooling becomes dominant. Compared with the above two cooling processes, the thermal emission from dust is extremely low and contributes only less than 0.1% to the total energy loss. The transition of nonradiative shock to radiative shock occurs when the cumulative energy loss reaches 0.01% of the explosion energy. Thus, only the H and He line cooling processes affect the time evolution of the nonradiative shock and the dust destruction efficiencies in the ISM with metallicity less than $Z = 10^{-4}\,Z_\odot$ corresponding to the dust-to-gas mass ratio of 4.5×10^{-7} in this paper.

However, the effects of cooling of gas by dust are expected to come to be important for the ISM with higher dust-to-gas mass ratio. The result of the calculation for dust destruction in the ISM with $Z = 10^{-4}\,Z_\odot$ and the dust-to-gas mass ratio 4.5×10^{-3} shows that the truncation time and the overall efficiency of dust destruction decrease by 4.4% and 2.6%, respectively, compared with the results for a dust-to-gas mass ratio of 4.5×10^{-7},

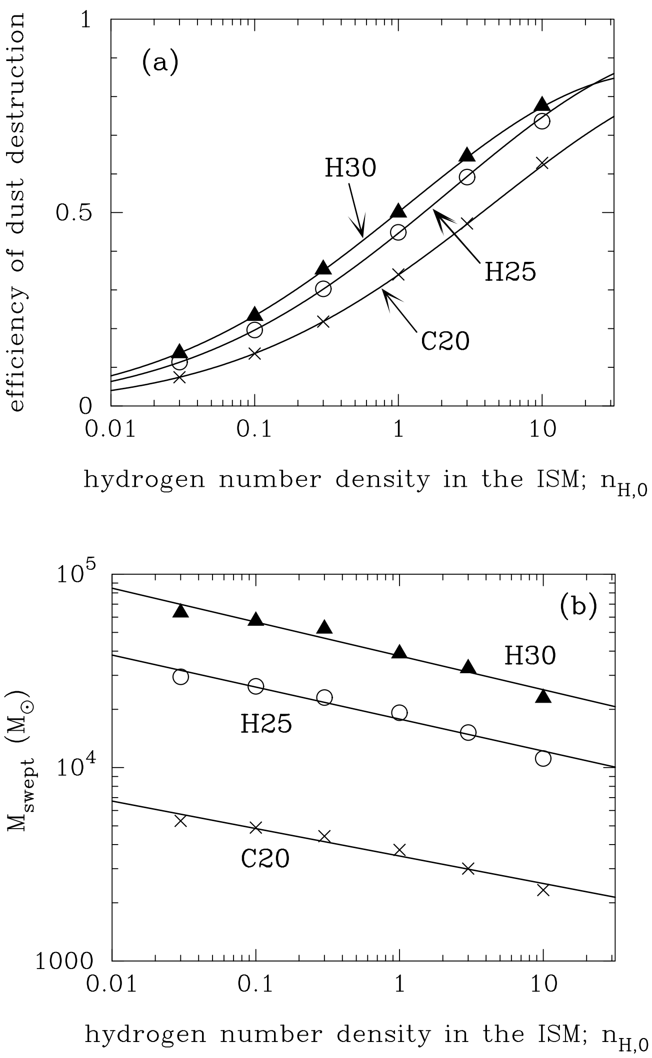

FIG. 10.—(*a*) Overall efficiency of dust destruction vs. $n_{\rm H,0}$ for models C20 (*crosses*), H25 (*open circles*), and H30 (*filled triangles*). The solid curves are calculated by the approximation formula of eq. (A3). (*b*) Mass of gas swept up by shock for models C20 (*crosses*), H25 (*open circles*), and H30 (*filled triangles*) as a function of $n_{\rm H,0}$. The linear lines are the power-law approximation formula of $M_{\rm swept} \propto n_{\rm H,0}^g$ with $g = -0.142E_{51}^{0.063}$. [*See the electronic edition of the Journal for a color version of this figure.*]

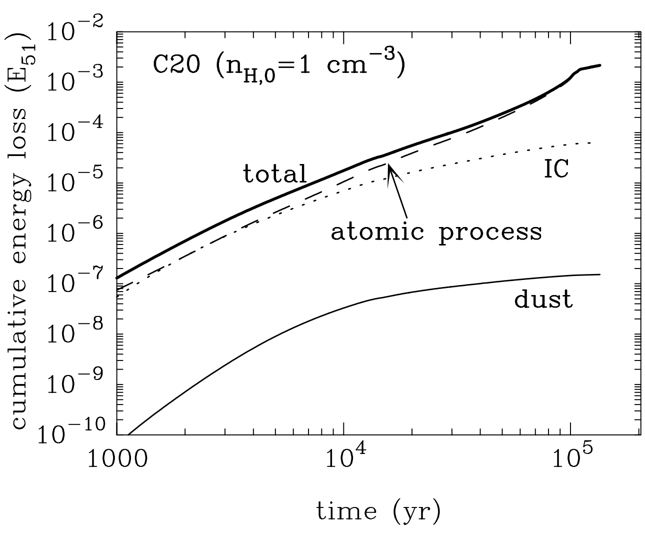

FIG. 11.—Time evolution of cumulative energy lost by the atomic process (*dashed line*), inverse Compton cooling (*dotted line*), and thermal emission from all dust grains (*thin solid line*) in units of E_{51} for the SN model C20, $n_{\rm H,0} = 1$, and $Z = 10^{-4}\,Z_\odot$ at a redshift of $z = 20$. The total energy loss is indicated by the thick solid curve. [*See the electronic edition of the Journal for a color version of this figure.*]

although the gas temperature in postshock gas decreases by about 20%. Even if the dust-to-gas mass ratio is raised by up to 4 orders of magnitude, the cooling of gas by dust in a nonradiative shock has significant effects on neither the efficiency of dust destruction nor the evolution of the nonradiative shock.

Furthermore, the inverse Compton cooling influences the evolution of nonradiative shocks in the early universe. Because the cooling rate by the inverse Compton scattering is proportional to $n_e T(1+z)^4$ and that by the atomic process is proportional to $n_e n_{\rm H} \sim n_{\rm H}^2$, the contribution of the inverse Compton cooling is enhanced in postshock flow with a lower gas density and/or higher gas temperature at higher redshift. At redshift $z = 40$, for the SN model C20 with preshock gas density of $n_{\rm H,0} = 1$ cm^{-3}, the truncation time is only 2% shorter than that calculated at $z = 20$. Thus, in this case, the inverse Compton cooling seems not to affect the destruction efficiency of dust grains. However, more systematic studies covering wide ranges of SN explosion energy and gas density in the ISM are necessary to reveal the effect of the inverse Compton cooling.

Note that the cooling function of gas for $Z = 10^{-3}\, Z_\odot$ is almost the same as that for the zero metal case (Sutherland & Dopita 1993). Thus, the parameters of the ISM considered in this paper ($Z = 10^{-4}\, Z_\odot$ and $z = 20$) are well fitted for investigating dust destruction in the early universe, and the timescale of dust destruction derived in § 7.2 is applicable over the wide ranges of metallicity of gas in the ISM ($Z \lesssim 10^{-3}\, Z_\odot$) and redshift ($z \leq 40$).

8. SUMMARY

We investigate the destruction of dust grains in the interstellar shocks driven by SNe as the second step to revealing the evolution of dust in the early universe, based on the dust models obtained by Nozawa et al. (2003). We focus on dust destruction in nonradiative shocks where dust grains are predominantly destroyed by nonthermal and thermal sputtering because of high temperature and high velocity of the gas. The sputtering yields for the combinations of dust and ion species of interest to us are evaluated by applying the universal relation for sputtering yield with a slight modification and by determining the value of K by fitting to the available experimental data and/or the results of the EDDY simulations. The modified universal relation derived here can present better fits to the available experimental data than the previous relation.

In the calculations of dust destruction, we solve the time evolution of gas temperature and density in spherically symmetric shocks, adopting the hydrodynamic models by Umeda & Nomoto (2002) as the initial conditions for interstellar shocks and including the cooling of gas by the atomic process, inverse Compton scattering, and the thermal emission of dust. The erosion of dust by thermal and nonthermal sputtering caused by motion of dust relative to gas is carefully treated by taking into account the size distribution of each dust species. The results of the calculations are summarized as follows.

1. Because the sputtering predominantly destroys the small grains, the number of small-sized grains such as Al_2O_3 and $MgSiO_3$ is greatly reduced. The erosion of C, SiO_2, and Fe grains whose size distributions are lognormal-like, with the average size larger than 0.01 μm, increases the numbers of smaller grains. The size distribution summed up over all grain species becomes flatter for small radius compared with the initial size distribution, while that for radius larger than 0.2 μm remains almost unchanged.

2. The efficiency of dust destruction is higher for the grains with a small average size such as Al_2O_3 and $MgSiO_3$ and with a power-law–like size distribution such as FeS, Mg_2SiO_4, and MgO. On the other hand, Si, Fe, C, and SiO_2 grains, which have a lognormal-like size distribution and a relatively large average radius, have a lower efficiency of destruction. A detailed analysis of the behavior of the dust destruction efficiency for each grain species indicates that not only sputtering yields but also the initial size distribution plays a crucial role in the efficiency of dust destruction by sputtering.

3. The efficiency of destruction ϵ_j for each dust species increases with increasing explosion energy E_{51} and/or increasing preshock gas density $n_{\rm H,0}$ but is almost independent of the progenitor mass $M_{\rm pr}$ of the SN as long as E_{51} remains the same. The destruction efficiency ϵ_j as a function of E_{51} is reproduced well by a power-law formula given by equation (A1). The dependence of ϵ_j on $n_{\rm H,0}$ is expressed well by the quadratic equation (A3) in terms of $\log n_{\rm H,0}$.

4. As is also the case for ϵ_j, the mass of gas swept up by the shock wave, $M_{\rm swept}$, is an increasing function of E_{51} and is approximated by a power-law formula given by equation (A2). However, $M_{\rm swept}$ decreases with increasing gas density in the ISM, and its dependence is also reproduced by a power-law formula whose index is given by equation (A4) as a function of E_{51}. Finally, by combining these results, we present an analytic formula for the timescale of destruction for each grain species in the early universe as a function of E_{51} and $n_{\rm H,0}$. The derived timescale of dust destruction can be used to investigate the time evolution of the amount of dust grains in the early universe.

5. In the early universe, only the H and He line cooling processes affect the time evolution of nonradiative shocks and the efficiency of dust destruction. The thermal emission from dust grains is not very important even for the ISM with a dust-to-gas mass ratio of $\sim 10^{-3}$ as long as the metallicity in the ISM is $Z \lesssim 10^{-3}\, Z_\odot$. In addition, inverse Compton cooling is expected not to have great effects on the evolution of shocks at high redshifts. Thus, the timescale of dust destruction derived in this paper is applicable for ranges of metallicity of gas in the ISM of $Z \lesssim 10^{-3}\, Z_\odot$ and redshift of $z \leq 40$.

In this study, we have focused on dust destruction in nonradiative shocks where dust grains in the ISM are considered to be predominantly destroyed. We should mention here that a part of the dust grains formed in the ejecta of SNe are expected to be destroyed by reverse shocks penetrating the ejecta. Because sputtering is the most dominant destruction process of dust grains in reverse shocks as well, the simulation code of dust destruction constructed in this paper can be applied to explore the destruction of dust grains by reverse shocks. This work is now in progress. Furthermore, in radiative shocks with shock velocities below 100 km s^{-1}, shattering and partial vaporization by grain-grain collisions become important in the presence of a magnetic field. A magnetic field frozen into the gas causes charged grains to gyrate and accelerate behind the shock front and results in the enhancement of not only the sputtering rate but also the grain-grain collision frequency. The shattering by grain-grain collision mainly leads to the redistribution of grain sizes (Tielens et al. 1994; Jones et al. 1996). The sophisticated study of this subject is left for future work.

The authors are grateful to the anonymous referee for critical comments, which have improved the manuscript. The authors thank H. Umeda and K. Nomoto for making the ejecta model of Population III supernovae available. This work has been supported in part by a Grant-in-Aid for Scientific Research from the Japan Society for the Promotion of Sciences (16340051).

TABLE 7

Coefficients for $M_{\rm swept}$ of the Approximation Formula (A2)

Coefficient	For all SNe	For SNe II	For PISNe
a_2	4.144E+03	4.118E+03	4.481E+03
b_2	7.967E−01	6.627E−01	8.864E−01

APPENDIX

THE APPROXIMATION FORMULAE FOR ϵ_j AND $M_{\rm swept}$

In this appendix, we present the approximate formulae for the efficiency of dust destruction ϵ_j and the mass of the gas swept up by the shock, $M_{\rm swept}$, as a function of the SN explosion energy E_{51} and the gas density $n_{\rm H,0}$ in the ISM. The energy dependence of the destruction efficiency for each grain species can be reproduced well by a power-law formula given by

$$\epsilon_j = a_{1,j} E_{51}^{b_{1,j}}. \tag{A1}$$

The solid lines in Figure 8 indicate the least-squares fits by this power-law formula for all SNe whose numerical coefficients $a_{1,j}$ and $b_{1,j}$ are tabulated in Table 6. The dependence of $M_{\rm swept}$ on E_{51} is well fitted by the power-law formula

$$M_{\rm swept} = a_2 E_{51}^{b_2} \tag{A2}$$

using the coefficients a_2 and b_2 given in Table 7 and is depicted in Figure 9 for all SNe (*solid line*), SNe II (*dotted line*), and PISNe (*dashed line*). The destruction efficiency ϵ_j for each grain species j as a function of $n_{\rm H,0}$, as well as the overall destruction efficiency, is expressed by

$$\log \epsilon_j = c_j (\log n_{\rm H,0})^2 + d_j \log n_{\rm H,0} + e_j, \tag{A3}$$

and the coefficients c_j, d_j, and e_j derived by the least-squares fits are given in Table 8 for models C20, H25, and H30, respectively, along with the coefficients for overall destruction efficiency. The solid curves in Figure 10*a* depict the overall destruction efficiencies calculated by equation (A3) for models C20, H25, and H30. This formula reproduces the destruction efficiencies calculated by the simulations with an accuracy of within less than 10% for $n_{\rm H,0} \leq 10\ {\rm cm^{-3}}$. The calculated $M_{\rm swept}$ can be reproduced by the power-law formula $M_{\rm swept} \propto n_{\rm H,0}^{g}$, where the index g is weakly dependent on E_{51} and is approximated by

$$g = -0.142 E_{51}^{0.063}. \tag{A4}$$

This formula produces good agreement with the results of the simulations, as represented by the solid lines in Figure 10*b*.

TABLE 8

Coefficients for the Approximation (A3)

	C20			H25			H30		
Dust Species	c_j	d_j	e_j	c_j	d_j	e_j	c_j	d_j	e_j
C	−0.062	0.41	−0.61	−0.07	0.36	−0.46	−0.08	0.33	−0.39
Si	−0.044	0.54	−0.87	−0.06	0.50	−0.67	−0.072	0.47	−0.58
Fe	−0.057	0.55	−0.81	−0.078	0.49	−0.61	−0.096	0.46	−0.51
FeS	−0.088	0.23	−0.23	−0.077	0.18	−0.16	−0.073	0.16	−0.13
Al_2O_3	−0.031	0.14	−0.17	−0.030	0.12	−0.13	−0.032	0.11	−0.11
$MgSiO_3$	−0.060	0.18	−0.19	−0.057	0.14	−0.13	−0.055	0.12	−0.11
Mg_2SiO_4	−0.087	0.31	−0.35	−0.092	0.25	−0.24	−0.097	0.22	−0.19
SiO_2	−0.086	0.33	−0.39	−0.093	0.27	−0.27	−0.097	0.24	−0.22
MgO	−0.079	0.29	−0.30	−0.086	0.23	−0.20	−0.089	0.20	−0.16
Overall	−0.067	0.33	−0.47	−0.067	0.29	−0.35	−0.072	0.26	−0.30

REFERENCES

Andersen, H. H., & Bay, H. L. 1981, in Sputtering by Particle Bombardment I, ed. R. Behrisch (Berlin: Springer), 145
Bach, H. 1970, Nucl. Instrum. Methods, 84, 4
Bach, H., Kitzmann, I., & Schroder, H. 1974, Radiat. Effects, 21, 31
Baines, M. J., Williams, I. P., & Asebiomo, A. S. 1965, MNRAS, 130, 63
Bertoldi, F., Carilli, C. L., Cox, P., Fan, X., Strauss, M. A., Beelen, A., Omont, A., & Zylka, R. 2003, A&A, 406, L55
Bianchi, S., & Ferrara, A. 2005, MNRAS, 358, 379
Blank, P., & Wittmaack, K. 1979, J. Appl. Phys., 50, 1519
Bohdansky, J. 1984, Nucl. Instrum. Methods Phys. Res. B, 2, 587
Bohdansky, J., Bay, H. L., & Ottenberger, W. 1978, J. Nucl. Math., 76–77, 163
Bohdansky, J., Bay, H. L., & Roth, J. 1977, In Proc. 7th Int. Vacuum Cong. and 3rd Int. Conf. on Solid Surfaces, ed. R. Dobrozemsky et al. (Vienna: R. Dobrozemsky et al.), 1509
Bohdansky, J., Roth, J., & Bay, H. L. 1980, J. Appl. Phys., 51, 2861
Bohdansky, J., Roth, J., & Sinha, M. K. 1976, in Proc. 9th Symp. on Fusion Technology (London: Pergamon), 541
Bromm, V., & Larson, R. B. 2004, ARA&A, 42, 79
Cazaux, S., & Spaans, M. 2004, ApJ, 611, 40
Chase, M. W., Davies, C. A., Downey, J. R., Frurip, D. J., McDonald, R. A., & Syverud, A. N. 1985, J. Phys. Chem. Ref. Data, 14, Suppl. 1
Coburn, J. W., Winters, H. F., & Chuang, T. J. 1977, J. Appl. Phys., 48, 3532
Draine, B. T., & Salpeter, E. E. 1979, ApJ, 231, 77
Dwek, E. 1987, ApJ, 322, 812
———. 1998, ApJ, 501, 643
Dwek, E., & Arendt, R. G. 1992, ARA&A, 30, 11
Dwek, E., Foster, S. M., & Vancura, O. 1996, ApJ, 457, 244
Edwin, R. P. 1973, J. Phys. D, 6, 833
Eernisse, E. P. 1971, J. Appl. Phys., 42, 480
Field, D., May, P. W., Pineau des Forêts, G., & Flower, D. R. 1997, MNRAS, 285, 839
Gnedin, N. Y., Ferrara, A., & Zweibel, E. G. 2000, ApJ, 539, 505
Hauser, M. G., & Dwek, E. 2001, ARA&A, 39, 249
Hechtl, E., Bohdansky, J., & Roth, J. 1981, J. Nucl. Math., 103–104, 333
Heger, A., & Woosley, S. E. 2002, ApJ, 567, 532
Hirashita, H., & Ferrara, A. 2002, MNRAS, 337, 921
Hirashita, H., Nozawa, T., Kozasa, T., Ishii, T. T., & Takeuchi, T. T. 2005, MNRAS, 357, 1077
Ikeuchi, S., & Ostriker, J. P. 1986, ApJ, 301, 522
Iskef, H., Cunningham, J. W., & Watt, D. E. 1983, Phys. Med. Biol., 28, 535
Jones, A. P., Tielens, A. G. G. M., & Hollenbach, D. J. 1996, ApJ, 469, 740
Jones, A. P., Tielens, A. G. G. M., Hollenbach, D. J., & McKee, C. F. 1994, ApJ, 433, 797
Kitayama, T., Yoshida, N., Susa, H., & Umemura, M. 2004, ApJ, 613, 631
Kozasa, T., Hasegawa, H., & Nomoto, K. 1989, ApJ, 344, 325
Laegreid, N., & Wehner, G. K. 1961, J. Appl. Phys., 32, 365
Loeb, A., & Haiman, Z. 1997, ApJ, 490, 571
Machida, M. N., Tomisaka, K., Nakamura, F., & Fujimoto, M. Y. 2005, ApJ, 622, 39
Maiolino, R., Oliva, E., Ghinassi, F., Pedani, M., Mannucci, F., Mujica, R., & Juarez, Y. 2004a, A&A, 420, 889
Maiolino, R., Schneider, R., Oliva, E., Bianchi, S., Ferrara, A., Mannucci, F., Pedani, M., & Roca Sogorb, M. 2004b, Nature, 431, 533
Mair, G., Müllar, E., Hillebrandt, W., & Arnold, C. N. 1988, A&A, 199, 114
Matsunami, N., Yamamura, Y., Itakawa, W., Itoh, N., Kazumata, Y., Myagawa, S., Morita, K., & Shimizu, R. 1980, Radiat. Effects Lett., 57, 15
May, P. W., Pineau des Forets, G., Flower, D. R., Field, D., Allan, N. L., & Purton, J. A. 2000, MNRAS, 318, 809
McKee, C. F. 1989, in Interstellar Dust, ed. L. J. Allamandora & A. G. G. M. Tielens (Dordrechent: Kluwer), 431
McKee, C. F., Hollenbach, D. J., Seab, C. G., & Tielens, A. G. G. M. 1987, ApJ, 318, 674
Nenadovic, T., Perraillon, B., Bogdanov, Z., Djordjevic, Z., & Milic, M. 1990, Nucl. Instrum. Methods Phys. Res. B, 48, 538
Nozawa, T., Kozasa, T., Umeda, H., Maeda, K., & Nomoto, K. 2003, ApJ, 598, 785
Ohya, K., & Kawata, J. 1997, Japanese J. Appl. Phys., 36, L298
Omukai, K., Tsuribe, T., Schneider, R., & Ferrara, A. 2005, ApJ, 626, 627
Priddey, R. S., Isaak, K. G., McMahon, R. G., Robson, E. I., & Pearson, C. P. 2003, MNRAS, 344, L74
Robson, I., Priddey, R. S., Isaak, K. G., & McMahon, R. G. 2004, MNRAS, 351, L29
Rosenberg, D., & Wehner, G. K. 1962, J. Appl. Phys., 33, 1842
Roth, J. 1983, in Sputtering by Particle Bombardment II, ed. R. Behrisch (Berlin: Springer), 91
Roth, J., Bohdansky, J., & Ottenberger, W. 1979, Rep. IPP 9/26 (Garching: MPI)
Schneider, R., Ferrara, A., Natarajan, P., & Omukai, K. 2002, ApJ, 571, 30
Schneider, R., Ferrara, A., & Salvaterra, R. 2004, MNRAS, 351, 1379
Schneider, R., Ferrara, A., Salvaterra, R., Omukai, K., & Bromm, V. 2003, Nature, 422, 869
Sigmund, P. 1969, Phys. Rev., 184, 383
———. 1981, in Sputtering by Particle Bombardment I, ed. R. Behrisch (Berlin; Springer), 9
Sommerfeldt, H., Mashkova, E. S., & Molchanov, V. A. 1972, Phys. Lett. A, 38, 237
Southern, A. L., Willis, W. R., & Robinson, M. T. 1963, J. Appl. Phys., 34, 153
Sutherland, R. S., & Dopita, M. A. 1993, ApJS, 88, 253
Tabata, T., Ito, R., & Okabe, S. 1972, Nucl. Instrum. Methods, 103, 85
Takeuchi, T. T., Hirashita, H., Ishii, T. T., Hunt, L. K., & Ferrara, A. 2003, MNRAS, 343, 839
Takeuchi, T. T., Ishii, T. T., Nozawa, T., Kozasa, T., & Hirashita, H. 2005, MNRAS, 362, 592
Tan, J. C., & McKee, C. F. 2004, ApJ, 603, 383
Tielens, A. G. G. M., McKee, C. F., Seab, C. G., & Hollenbach, D. J. 1994, ApJ, 431, 321
Todini, P., & Ferrara, A. 2001, MNRAS, 325, 726
Umeda, H., & Nomoto, K. 2002, ApJ, 565, 385
van Albada, G. D., van Leer, B., & Roberts, W. W., Jr. 1982, A&A, 108, 76
Vanzi, L., Hunt, L. K., Thuan, T. X., & Izotov, Y. I. 2000, A&A, 363, 493
von Seefeld, H., Schmidl, H., Behrisch, R., & Scherzer, B. M. U. 1976, J. Nucl. Math., 63, 215
Wolfire, M. G., Hollenbach, D., McKee, C. F., Tielens, A. G. G. M., & Bakes, E. L. O. 1995, ApJ, 443, 152
Ziegler, J. F., Biersack, J. P., & Littmark, U. 1985, The Stopping and Range of Ions in Solids (New York: Pergamon)